International Journal of Multiphase Flow 189 (2025) 105244

Contents lists available at ScienceDirect

International Journal of Multiphase Flow

journal homepage: www.elsevier.com/locate/ijmulflow

Numerical Simulations of bubbly turbulent convection in cubical geometries

Joauma Marichal [a],*, Yann Bartosiewicz [a], Pierre Ruyer [b]

[a] Université catholique de Louvain, Institute of Mechanics, Materials and Civil Engineering, Louvain-la-Neuve, 1348, Belgium

[b] Autorité de Sûreté Nucléaire et de Radioprotection (ASNR), PSN-RES/SEMIA, Saint-Paul-Lez-Durance, F-13115, France

ARTICLE INFO

Keywords:
Rayleigh–Bénard
Bubble dynamics
Two-way coupling
Convection

ABSTRACT

In this work we present numerical results of bubble dynamics in a turbulent Rayleigh–Bénard convection configuration, using our in-house code in a cubical geometry. The problem in hand is encountered in various natural phenomena as well as in industrial applications. A Eulerian–Lagrangian approach is developed for the mixture of liquid water and vapor bubbles. The liquid mean temperature is close to the saturation temperature and is governed by the quasi-incompressible Navier–Stokes equations that are solved using Direct Numerical Simulations (DNS) standards. The motion and growth/shrinkage of each individual vapor bubble is modeled and the effect of the bubbles on the fluid is accounted via momentum and energy exchanges between the two phases (two-way coupling).

At first, we describe the model used and its corresponding validation, involving isolated bubble dynamics and coupling between bubbly and bulk flows. In the second part, we consider the study of the flow topology, the bubble related statistics, the heat transfer (Nusselt number) and the turbulence statistics for different settings of the bubbly configurations.

1. Introduction

Rayleigh–Bénard convection (RBC) is a well-known buoyancy-driven flow of a fluid confined between a hot lower wall at temperature T_{hot} and a cold upper wall at temperature T_{cold}. It has been extensively studied in the literature; see for example (Cioni et al., 1996, 1997; Krishnamurti and Howard, 1981; Niemela et al., 2000; Pallarès et al., 2001; Pallares et al., 1996; Zhou and Xia, 2013) and references therein. The problem is governed by three dimensionless parameters: the Rayleigh number Ra, the Prandtl number Pr, and the aspect ratio Γ of the enclosure. The Rayleigh number characterizes the fluid flow regime (laminar versus turbulent) and is the ratio of buoyancy forces to viscous forces, otherwise known as the Grashof number, multiplied by the Prandtl number. The latter is a property of the fluid which indicates the relative importance of momentum versus thermal diffusion. The aspect ratio is defined as the ratio of the horizontal to vertical dimensions of the geometry. In cubical geometries (Vishnu et al., 2020; Foroozani et al., 2017), the flow has been shown to present a main convection cell, called the Large Scale Circulation (LSC), which is aligned to one of the diagonal plane of the domain. In the second diagonal, four counter-rotating vortices interact with each another. Research on the subject has also provided important information and physical insight on the properties of the thermal and hydrodynamic boundary layers and the turbulence statistics. The dependence between the heat flux through the domain, i.e. the Nusselt number, and the governing parameters have been characterized by correlations (Niemela et al., 2000; Hay et al., 2021).

This study builds on these foundational findings by introducing the presence of vapor bubbles to the flow as boiling RBC is a common phenomenon in various technological applications. Notably in nuclear spent fuel pools during loss-of-cooling accidents, as highlighted and studied experimentally by Martin et al. (2023). We therefore perform Direct Numerical Simulations (DNS) of a two-phase flow composed of water, close to its saturation temperature, and vapor bubbles; namely a pool boiling configuration at atmospheric pressure.

To handle this two-phase flow, we considered three possible modeling approaches, each focusing on different time and length scales. The first is the microscopic approach (Ganguli and Kenig, 2011; Juric and Tryggvason, 1998; Gennari et al., 2024), which solves both phases as separate continua and tracks the interface that separates them. This approach is capable of capturing nucleation, collapse, and interfacial transfer dynamics, However, it is limited to a single or a few bubbles due to the high numerical costs involved. The second approach is the Eulerian–Eulerian model (Ferrante and Elghobashi, 2007; Deen et al., 2004), which treats the two phases as interpenetrating continua and represents the bubbles as a statistical population. This method is not limited by the number of bubbles but requires closure models to capture

* Corresponding author.
E-mail address: joauma.marichal@uclouvain.be (J. Marichal).

https://doi.org/10.1016/j.ijmultiphaseflow.2025.105244
Received 23 December 2024; Received in revised form 13 March 2025; Accepted 4 April 2025
Available online 15 April 2025
0301-9322/

complex interactions. While it can simulate large bubble populations, it is less focused on the detailed dynamics of individual bubbles.

We opted for the third choice, the Eulerian–Lagrangian approach, which combines the strengths of both previous models and is well-suited for simulating bubbly flows with a relatively large number of bubbles while still capturing their individual dynamics. In this approach, the fluid phase is solved using the Navier–Stokes equations, while each bubble's position, velocity, and radius are tracked separately, allowing to capture the influence of bubbles on the fluid as well as bubble-bubble interactions (not performed here). The Eulerian–Lagrangian approach has been used within various scopes of work, notably to simulate solid particles in channel flows (Lessani and Nakhaei, 2013), bubbly flows in complex geometries in order to assess cavitation issues (Shams et al., 2011; Shams, 2009), bubbles in a 2D Taylor–Green vortex (Ferrante and Elghobashi, 2007), bubbles in a laminar channel flow (Tomiyama et al., 1997), buoyancy driven bubbles in a quiescent fluid with collisions between bubbles (Darmana et al., 2006), bubbles in a quiescent fluid column with coalescence models (Deen et al., 2004) and, most similar to what is done in this paper, bubbly Rayleigh–Bénard convection in cylindrical geometries (Lakkaraju, 2012; Oresta et al., 2009; Schmidt et al., 2011). The key advantage of this method is that bubbles are not only influenced by the fluid flow, but also impact the surrounding fluid through additional source terms. This specificity is called two-way coupling, as opposed to one-way coupling where the fluid does not consider the bubbles (Elghobashi, 1994). The two-way coupling terms account for the force that a bubble applies on, and the energy that a bubble exchanges with the surrounding liquid. Additionally, this model includes bubble growth and decay, tracked using a heat balance equation and controlled by a dimensionless parameter, the Jakob number Ja_b which quantifies the relative enthalpy difference between the liquid and its saturation state in comparison to the latent heat.

The primary aim of this study is to investigate the effects of vapor bubbles on turbulent Rayleigh–Bénard convection in a cubical geometry with a focus on the interaction between the fluid phase and vapor bubbles. Specifically, we analyze the impact of the amount of bubbles and of the Jakob number on flow topology, turbulence statistics, and heat transfer mechanisms. To that end, simulations of bubbly RBC are carried out for water with a Rayleigh number of 2.12×10^5 and an aspect ratio of $1/2$. These simulations are run with our in-house code relying on the previously described Eulerian-Lagrangian model. While our model provides valuable insights, it has certain limitations, including the neglect of bubble-bubble interactions and volumetric coupling effects. As such, we focus on dilute bubble fractions where these assumptions remain reasonable, but they should be considered when interpreting the results.

The paper is structured as follows. In Section 2 we present the mathematical models for the fluid phase, the bubbles and their interactions. Then, in Section 3, we present a validation and verification procedure against analytical, experimental and numerical results. Section 4 describes the governing parameters of the flow under study and the numerical set-up of our simulations. Section 5 contains the presentation and analysis of numerical results, where we first explain the global structure of the flow before elaborating on more specific bubble/fluid related statistics. Subsequently, we discuss the various way's of steering the Jakob's number, see Section 6. Finally, conclusions are drawn in Section 7.

2. Model

This section focuses on describing the models used to simulate the two-phase flow of interest. It first details each phase individually, i.e. liquid and vapor, before investigating their interactions.

2.1. Fluid equations

The fluid is governed by the quasi-incompressible Navier–Stokes–Fourier equations. The effects of vapor bubbles on the fluid are reflected through additional momentum ($\boldsymbol{f}_u$) and energy (f_T) terms (Darmana et al., 2006; Shams et al., 2011), while volumetric coupling is neglected. Accordingly, the equations read, in dimensional form,

$$\frac{\partial \rho}{\partial t} + \nabla\cdot(\rho \boldsymbol{u}) = 0\,, \tag{1}$$

$$\frac{\partial(\rho \boldsymbol{u})}{\partial t} + \nabla\cdot(\rho \boldsymbol{u}\boldsymbol{u}) = -\nabla p + \nabla\cdot(2\mu \boldsymbol{S}) + \rho \boldsymbol{g} + \boldsymbol{f}_u\,, \tag{2}$$

$$\frac{\partial(\rho c_p T)}{\partial t} + \nabla\cdot\left(\rho c_p \boldsymbol{u} T\right) = \frac{\partial p_0(t)}{\partial t} + \nabla\cdot(\kappa \nabla T) + f_T\,, \tag{3}$$

where ρ, $\boldsymbol{u}$ and T stand for density, velocity vector and temperature of the fluid respectively. $\boldsymbol{S}$ is the deviatoric component of the viscous stress tensor, $\boldsymbol{S} = \frac{1}{2}\left(\nabla \boldsymbol{u} + (\nabla \boldsymbol{u})^\top\right) - \frac{1}{3}(\nabla\cdot \boldsymbol{u})\mathbf{I}$ with $\mathbf{I}$ being the identity tensor and μ, c_p, κ are the fluid dynamic viscosity, specific heat capacity and thermal conductivity respectively. Furthermore, $\boldsymbol{g}$ denotes the gravitational acceleration.

The system of equations is closed thanks to an isobaric "equation of state" for $\rho(T)$ taking the form of a fifth order polynomial fit: $\rho(T) = 8.67e^2 + 1.02\,T - 7.66e^{-4}\,T^2 - 5.70e^{-6}\,T^3 + 5.83e^{-9}\,T^4$ (Lemmon et al., 2010). The latter allows pressure and density to be decoupled. The pressure can therefore be decomposed into two components. The first one is the thermodynamic pressure $p_0(t)$ which is spatially uniform and a function of time only. For the flows under study, p_0 is constant and equal to the ambient pressure. The second term is the dynamic pressure, p, as seen in Eq. (2). This formalism refers to the low Mach number assumption, used for quasi-incompressible fluids in convection problems (Paillere et al., 2000; Hay and Papalexandris, 2019).

The spatial discretization is performed on a collocated rectilinear grid using second order central differences and requires the implementation of a flux-interpolation scheme to prevent the odd–even decoupling of the pressure field (Hamtiaux, 2024; Rhie and Chow, 1983).

2.2. Bubbles

The bubbles, having smaller densities than the surrounding fluid, are subjected to the gravitational force, the undisturbed outer fluid forces, the drag force, the lift force, the added mass force and a force representing the momentum transfer due to size variations (Lakkaraju, 2012; Oresta et al., 2009; Shams et al., 2011; Elghobashi, 1994; Mazzitelli et al., 2003). The bubble radius is obtained by balancing the heat due to evaporation/condensation with the heat exchanged with the liquid (Lakkaraju, 2012; Oresta et al., 2009) while assuming that the bubble temperature T_b equals the saturation temperature, T_{sat} and the bubble density, ρ_b is constant (which makes the energy balance of the bubbles population trivial). Bubble–bubble collisions are neglected while bubble–wall collisions are modeled as elastic. The bubble position $\boldsymbol{x}_b$, bubble velocity $\boldsymbol{u}_b$ and bubble radius r_b time derivatives are given by,

$$\frac{d\boldsymbol{x}_b}{dt} = \boldsymbol{u}_b\,, \tag{4}$$

$$\begin{aligned}\rho_b V_b \frac{d\boldsymbol{u}_b}{dt} = {} & \underbrace{-\rho_b V_b \boldsymbol{g}}_{\text{Gravity, } F_{G,b}} \underbrace{+\rho V_b\left(\boldsymbol{g} + \frac{D\boldsymbol{u}}{Dt}\right)}_{\text{Undist. } F_{U,b}} \underbrace{-\frac{C_D}{2}\rho A_b |\boldsymbol{u}_b - \boldsymbol{u}|(\boldsymbol{u}_b - \boldsymbol{u})}_{\text{Drag, } F_{D,b}} \\ & \underbrace{-C_L \rho V_b(\boldsymbol{u}_b - \boldsymbol{u}) \times \nabla \times \boldsymbol{u}}_{\text{Lift, } F_{L,b}} \underbrace{-C_A \rho V_b\left(\frac{d\boldsymbol{u}_b}{dt} - \frac{D\boldsymbol{u}}{Dt}\right)}_{\text{Added Mass, } F_{AM,b}} \\ & \underbrace{+C_A \rho(\boldsymbol{u} - \boldsymbol{u}_b)\frac{d}{dt}\left(\frac{4}{3}\pi r_b^3\right)}_{\text{Size variation, } F_{\dot{r},b}},\end{aligned} \tag{5}$$

$$\frac{dr_b}{dt} = \frac{h_b}{h_{lv}\rho_b}(T - T_{sat}), \tag{6}$$

where $V_p = \frac{4}{3}\pi r_b^3$ denotes the bubble volume, $A_b = \pi r_b^2$ the bubble exposed frontal area, h_b the bubble–fluid heat transfer coefficient, h_{lv} the latent heat and C_D, C_L and C_A are the drag, lift and added mass coefficients respectively. The $\frac{D}{Dt}$ operator denotes the material derivative following a fluid element (Ferrante and Elghobashi, 2007; Darmana et al., 2006; Maxey and Riley, 1983; Magnaudet et al., 1995). The undisturbed outer fluid force, referred to as "Undist.", encompasses Archimedes' force, as well as a similar force that accounts for an analogous effect resulting from the acceleration of the undisturbed fluid (Maxey and Riley, 1983; Auton et al., 1988; Magnaudet, 1997) resulting in the "force exerted by the outer [undisturbed] flow on the volume of fluid occupied by the particle" as stated by Magnaudet (1997).

The lift and added mass coefficients are set to 1/2 (Lakkaraju, 2012). The drag coefficient (Oresta et al., 2009; Mei et al., 1994; Mei and Klausner, 1992) is modeled as,

$$C_D = \frac{16}{Re_b}\left(1 + \frac{Re_b}{8 + \frac{1}{2}(Re_b + 3.315\sqrt{Re_b})}\right), \tag{7}$$

where $Re_b = \frac{2\rho r_b |u - u_b|}{\mu}$ is the bubble Reynolds number. The bubble–fluid heat transfer coefficient, h_b is obtained thanks to the single-bubble Nusselt number, Nu_b as Oresta et al. (2009), Legendre et al. (1998) and Favre (2023),

$$h_b = \frac{\kappa Nu_b(Pr, Ja_b, Re_b)}{2r_b}. \tag{8}$$

The latter is function of the Prandtl number as well as the bubble Reynolds number (defined above) and bubble Jakob number,

$$Ja_b = \frac{\rho c_p (T - T_{sat})}{\rho_b h_{lv}}, \tag{9}$$

defined locally for each bubble. Correlations for the single-bubble Nusselt number are taken from Favre (2023) for locally sub-cooled and super-heated liquid respectively,

$$Nu_b(Pr, Ja_b, Re_b) = \begin{cases} \max\left(2, \frac{12}{\pi} Ja_b, 2\sqrt{\frac{Re_b Pr}{\pi}}\right) & \text{for } Ja_b \geq 0 \quad \text{(Bubble growth)}, \\ 2 + 0.6 Re_b^{\frac{1}{2}} Pr^{\frac{1}{3}} & \text{for } Ja_b < 0 \quad \text{(Bubble collapse)}. \end{cases} \tag{10}$$

2.3. Bubble–fluid interactions

An interpolation operator is needed to couple the two reference frames (respectively Eulerian and Lagrangian) in a smooth manner and ensuring the conservation of transferred variables (Darmana et al., 2006; Shams et al., 2011). The mapping from the Eulerian to the Lagrangian frame relies on Lagrange polynomials. For the reverse transformation, we rely on the work of Deen, Sint Annaland, and Kuipers (Deen et al., 2004) and we use a clipped fourth-order polynomial function,

$$\boldsymbol{\omega}(b) = \begin{cases} \frac{15}{16}\left[\frac{(\boldsymbol{x}-\boldsymbol{x}_b)^4}{n^5} - 2\frac{(\boldsymbol{x}-\boldsymbol{x}_b)^2}{n^3} + \frac{1}{n}\right] & -n \leq \boldsymbol{x} - \boldsymbol{x}_b \leq n, \\ 0 & \text{otherwise}, \end{cases} \tag{11}$$

where $\boldsymbol{x}$ and $\boldsymbol{x}_b$ denote the local and particles coordinates respectively. n is the half-width of the mapping window, which is defined as the distance separating the bubble from the nearest end of its neighboring cell. This mapping is illustrated in Fig. 1 and allows the effects of the bubbles to be distributed to their neighboring cells according to the proportions given by the integration of the clipped fourth-order polynomial function $\boldsymbol{\omega}_b$ on the affected cells. One should note that this process is limited by the number of ghost cells when running in parallel, in our case, one ghost cell.

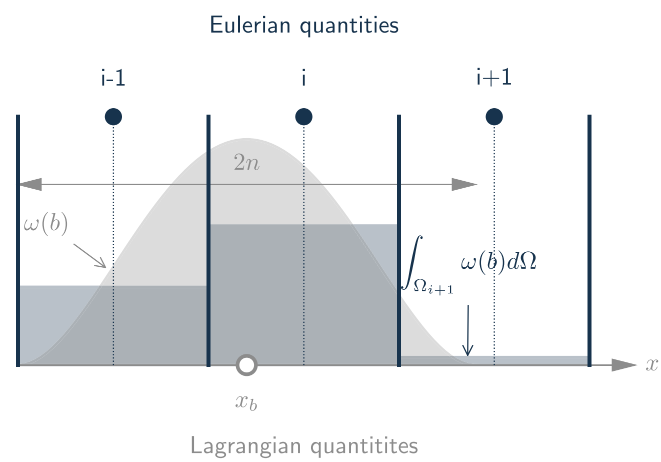

Fig. 1. Illustration of the mapping mechanism from the Lagrangian to the Eulerian frame.

Using the previously described mapping function, one can obtain the corresponding Eulerian quantities, ψ_E from the Lagrangian ones, ψ_L:

$$\psi_E(j) = \frac{\sum_b \psi_L(b) \int_{\Omega_j} \boldsymbol{\omega}(b) d\Omega}{V_{cell}}, \tag{12}$$

where j denotes the cells indices, b the bubbles indices and Ω_j the volume of the jth computational cell. This mapping enables us to obtain the last terms of Eqs. (2)–(3), accounting for the effects of bubbles on the fluid, which are therefore expressed as,

$$\boldsymbol{f}_u(j) = \frac{\sum_b \left(F_{G,b} + F_{D,b} + F_{L,b} + F_{AM,b} + F_{\dot{r},b}\right) \int_{\Omega_j} \boldsymbol{\omega}(b) d\Omega}{V_{cell}}, \tag{13}$$

$$f_T(j) = \frac{\sum_b \left(4\pi r_b^2 h_{b,b}(T_{sat} - T|_b)\right) \int_{\Omega_j} \boldsymbol{\omega}(b) d\Omega}{V_{cell}}. \tag{14}$$

It also allows to define other important flow parameters such as the bubble void fraction ϕ_b, which is defined as,

$$\phi_b(j) = \frac{\sum_b V_b(b) \int_{\Omega_j} \boldsymbol{\omega}(b) d\Omega}{V_{cell}}, \tag{15}$$

and the fluid volumetric fraction, ϕ, which is obtained through the following relation: $\phi + \phi_b = 1$. The volumetric fraction does not appear in Eqs. (1)–(3), as volumetric coupling is not taken into account in this study.

2.4. Time advancement

The fluid time step is limited by two factors. The first concerns the convergence of the solution of partial differential equations, and is based on the Courant number, C_0: $\Delta t_{C_0} = C_0 \min\left(\frac{\Delta x}{u_i}\right)$. The second is linked to the thermal nature of the problem, and more specifically to the time scale characteristic of heat diffusion. It is expressed as a function of the Fourier number, Fr, such that, $\Delta t_{Fr} = Fr Re \Delta x^2/\nu$. The bubbles, on the other hand present time scales associated with the drag and lift forces, $\tau_D^{-1} = \frac{3}{4} C_D \frac{|u_b - u_f|}{2r_b}$ and $\tau_L^{-1} = C_L |\nabla \times \boldsymbol{u}_f|$ respectively. As the time scales associated with the bubbles are smaller than the flow solver time step (Shams et al., 2011), a sub-cycling procedure for the bubbles is implemented where the fluid and bubbles time step are defined respectively as $\Delta t = min\left(\Delta t_{C_0}, \Delta t_{Fr}\right)$ and $\Delta t_b = \min\left(\frac{\Delta t}{3}, \tau_D, \tau_L\right)$.

Fig. 2 illustrates the algorithm for this Eulerian–Lagrangian approach. At each iteration, we start with the bubble subcycling procedure, where we update the bubble fields according to the previously computed bubble time-step. We then compute the corresponding effect of the bubbles, $\boldsymbol{f}_u$ and f_T, as well as the void fraction, ϕ. We finally

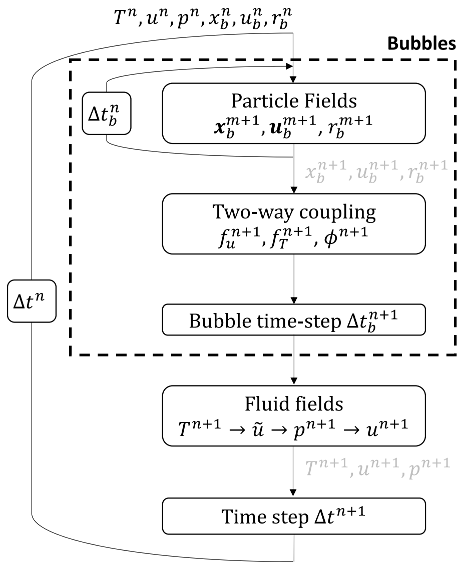

Fig. 2. Illustration of the algorithm.

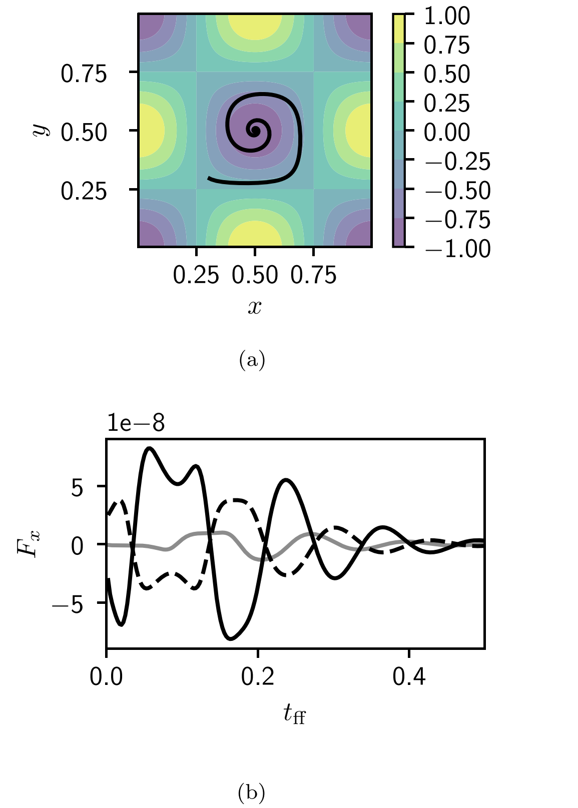

Fig. 3. (a) Instantaneous contours of the vorticity ω/ω_0 in the absence of bubbles at time $t_{\mathrm{ff}} = 0.2$ superimposed with a single bubble trajectory from 0 up to 2 t_{ff}. (b) Evolution of the drag (▬▬), lift (▬▬) and added-mass (▬ ▬ ▬) forces acting on the bubble. (For interpretation of the references to color in this figure legend, the reader is referred to the web version of this article.)

determine the new time step required by each bubble, Δt_b^{n+1}. The fluid phase is then solved using a PISO-type projection method.

3. Validation

A series of test cases are made to validate the in-house code used. The first section relies on Taylor–Green vortices. A single particle's trajectory is analyzed without taking into account the force of gravity or heat transfer. Afterward, the effects of two-way coupling are studied in similar condition with approximately 200 000 bubbles. The second section focuses on gravity effects, by adding a single bubble in a fluid at rest without and with radius variations. Finally, the thermal effects on a single bubble are analyzed. In all of the above tests, we compare our results with experimental data, theoretical results and/or other numerical simulations. For purposes of non-dimensionalization, the free-fall time $t_{\mathrm{ff}} = h/u_{\mathrm{ff}}$ is used as the reference time unit with the free-fall velocity, u_{ff} fixed to unity.

3.1. Taylor–Green vortex

A two-dimensional Taylor–Green vortex (Taylor and Green, 1937), which can be seen as an array of counter-rotating vortices, is studied in the presence of bubbles. The Taylor–Green vortex has been extensively used as validation for numerical methods thanks to its analytical solution. The problem does not consider the energy equation, bubble growth or gravity effects which are therefore neglected in this section. The initial fluid conditions are given by:

$$u_x(x,y) = -\frac{\omega_0}{2k}\cos(kx)\sin(ky) \quad \text{and} \quad u_y(x,y) = \frac{\omega_0}{2k}\sin(kx)\cos(ky)\,, \tag{16}$$

where $\omega_0 = 100$ is the initial maximum vorticity and $k = 2\pi$ is the wave number. The initial bubble velocities are set to that of the fluid at the respective location. The drag coefficient is simplified to $C_D = 24/Re_b$. The domain is periodic and the mesh uniform with 125 × 125 cells. Such flow is illustrated by the color plot of Fig. 3(a) in the absence of bubbles.

A first test case is performed to analyze the motion of a single bubble in the aforementioned vortex. This test case is inspired by Shams et al. (2011), which performed a similar analysis in a Rankine vortex. We decided to use a Taylor–Green vortex as to keep a Cartesian domain. The single bubble is initially located at the bottom left corner of the central vortex, $(x, y) = (0.3, 0.3)$ and is subject to drag, lift and added-mass forces. Fig. 3(a) displays the trajectory of the bubble. The color-plot of the vorticity in the absence of bubbles is also shown. The bubble follows a spiral trajectory towards the center of the domain (i.e., center of the center vortex). This movement is mainly due to the drag and added-mass forces, as illustrated by Fig. 3(b).

The influence of the Stokes number, $St = \omega_0 \rho r_b^2/9\mu$, on the bubble trajectory can be seen in Fig. 4. As the particle's size decreases, it takes more time to reach the center. The above results are in agreement with the ones of Shams et al. (2011).

A second test case is performed to study the effect of bubbles on the liquid phase. 230 400 bubbles are evenly distributed in space, leading to a uniform bubble void fraction of $\phi_{b,0} = 0.01$. The bubbles migrate towards the center of the vortical structures and modify the flow significantly. To enable comparison with previous studies, volumetric coupling has been added here. The effects of vapor bubbles on the fluid (i.e., two-way coupling) are reflected in the volume fraction of the liquid phase as well as in the additional momentum and energy terms. The system of equations (Eqs. (1)–(3)) is modified to account for the fluid void fraction, ϕ in a similar way as what has been done by Darmana et al. (2006) and Shams et al. (2011). Figs. 5 and 6 display the instantaneous contours of the vorticity and bubble concentration respectively, showing the influence of the bubbles on the flow and their distribution within it.

Fig. 7(a) shows the bubble void fraction at the center of the domain with time for one-way coupling and two-way coupling (volumetric coupling and additional momentum). Our results agree well with the ones obtained by two previous studies (Ferrante and Elghobashi, 2007; Shams et al., 2011). As discussed in Shams et al. (2011), the slight

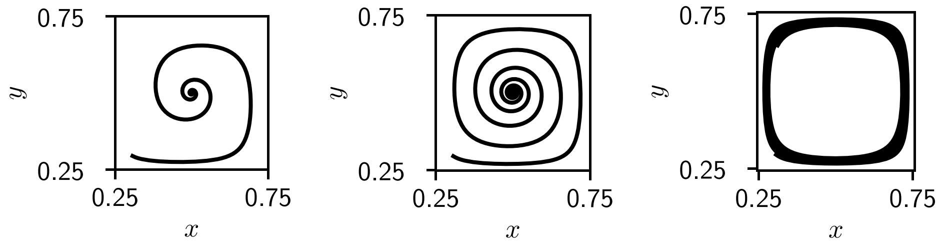

(a) (b) (c)

Fig. 4. Single bubble trajectories for Stokes number (a) $St = 0.02$, (b) $St = 0.01$ and (c) $St = 0.001$.

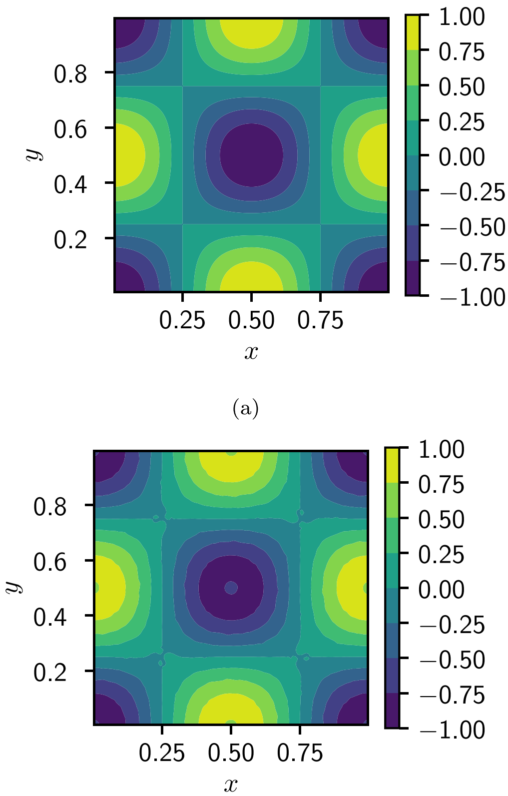

(a)

(b)

Fig. 5. Instantaneous contours of the vorticity ω/ω_0 at time $t_{ff} = 0.2$ for (a) single phase and (b) 230 400 bubbles with two-way coupling: volumetric coupling and additional momentum.

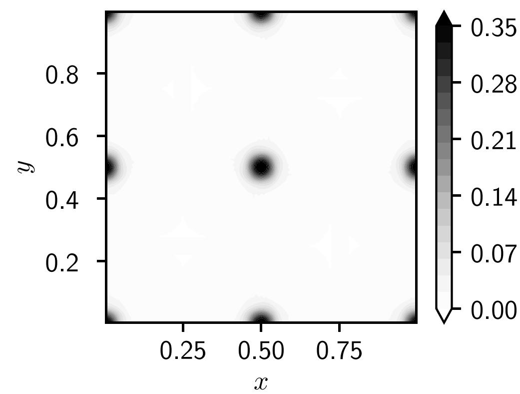

Fig. 6. Instantaneous contours of the bubble concentration ϕ_b at time $t_{ff} = 0.2$ for two-way coupling (volumetric coupling and additional momentum).

differences are explained by differences of numerical schemes and interpolation methods. Fig. 7(b) presents the vorticity at the center of the domain with time again for one-way and two-way coupling (volumetric coupling and additional momentum). The one-way coupling results in a constant unit value, which matches perfectly with the value that can be derived from the analytical solution of the Taylor–Green vortex (see Eqs (16)). The two-coupling coupling results are in line with those previously obtained in the literature. A decrease in vorticity at the center of the domain is observed and explained by the increase in friction between bubbles and liquid, reducing the latter's rotation.

3.2. Single rising bubble

To study the effects of gravity on a single bubble, another test case is carried out. A single rising bubble is placed in a quiescent fluid. Theoretically, the bubble reaches its terminal velocity, which is obtained by equalizing the forces of drag and gravity (only forces present in a fluid at rest with a bubble rising at a constant velocity and with a fixed radius): $u_{\mathrm{ter}} = (\rho - \rho_b) g \frac{2r_b^2}{\mu}$.

Fig. 8(a) displays the velocity of the single particle as a function of time. The particle follows a rectilinear vertical trajectory (Bonnefis et al., 2023) and its vertical velocity tends towards the theoretical terminal velocity (Shams et al., 2011). The density and viscosity of the fluid are set to $\rho = 1000$ [kg/m^3] and $\mu = 0.001$ [kg/ms], while the bubble has a density of $\rho_b = 1$ [kg/m^3] and a radius set to $r_b = 0.5$ [mm]. One should note that the drag coefficient is simplified to $C_D = 24/Re_b$.

A similar test case is performed, taking into account any change in bubble radius due to pressure. The ideal gas law establishes the following relation: $pV = nRT$ where p, V and T are the pressure, volume and temperature respectively, n is the amount of substance and $R = 8.314 \frac{\mathrm{J}}{\mathrm{mol\ K}}$ is the ideal gas constant. The amount of substance contained in a bubble is therefore computed using the initial pressure and radius as $n = \frac{p\frac{4}{3}\pi r_{b,0}^3}{RT}$. The pressure is defined as $p = p_{\mathrm{atm}} + \rho g y$ and p_{atm} is set to the low value of 1000 [Pa], in order to see some change in the bubble size. The bubble radius is therefore re-computed at each iteration as, $r_b = \left(\frac{3nRT}{4\pi p}\right)^{1/3}$. Fig. 8(b) displays the velocity of the bubble with time. As times passes, the radius increases and so does the velocity. The actual speed stays slightly below the theoretical terminal speed. This discrepancy arises because the terminal velocity depends on the bubble radius, which increases over time. However, the bubbles grow more rapidly than they are able to reach their corresponding terminal velocity. As a result, the actual velocity lags behind the theoretical terminal velocity, especially as the radius changes more rapidly. The forces acting on the bubble are displayed in Fig. 9. The drag and gravity forces counterbalance one another and as the bubble size increases, the momentum transfer due to radius variation grows in importance.

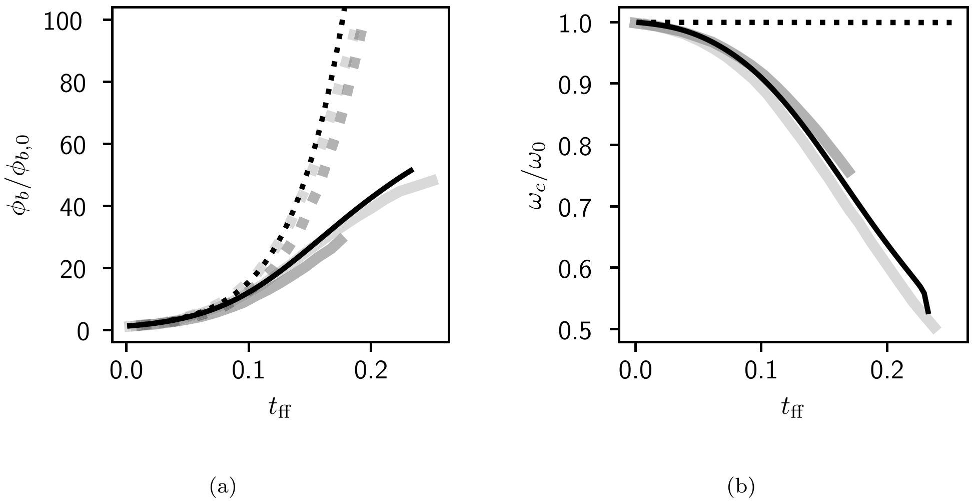

Fig. 7. (a) Normalized bubble void fraction and (b) normalized vorticity; at the vortex center for one-way coupling (▪▪▪▪) and two-way coupling, volumetric coupling and additional momentum (▬▬). Results from Ferrante and Elghobashi (2007) (▮ ▮ ▮ – ▬▬) and Shams et al. (2011) (▮ ▮ ▮ – ▬▬), for one and two-way coupling respectively, are added for comparison.

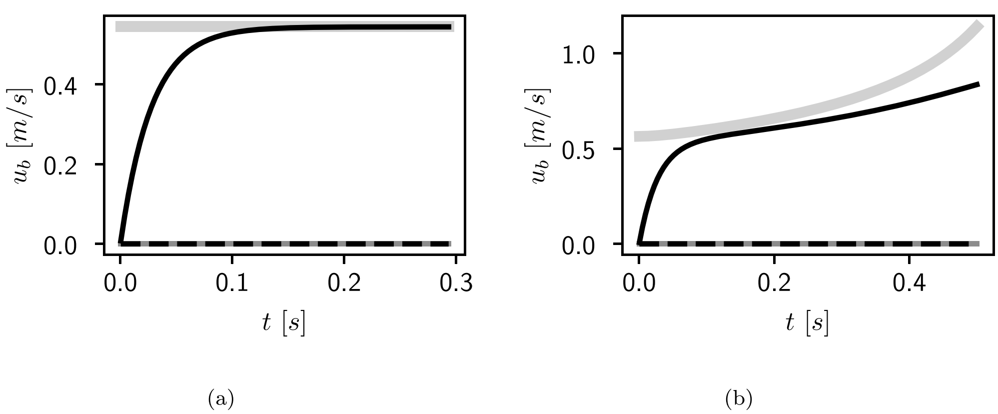

Fig. 8. Velocity of a single bubble in a quiescent liquid: u_x (▬▬), u_y (▬▬) and u_z (▬ ▬ ▬) and the theoretical terminal velocity (▬▬) for a bubble (a) without and (b) with radius variation.

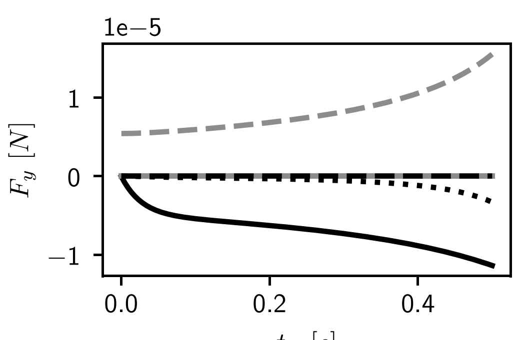

Fig. 9. Forces on a single bubble in a quiescent fluid: drag (▬▬), lift (▬▬), added mass (▬ ▬ ▬), gravity (▬ ▬ ▬) and radius variations (▪▪▪▪).

3.3. Bubble growth in a super-heated liquid

To analyze the thermal aspect of bubbles, we consider a single bubble at rest in a super-heated liquid, also at rest. The liquid is initially at a super-heated temperature T_0 which is kept constant through time. This problem has been studied theoretically and experimentally by Plesset and Zwick (1954) and Dergarabedian (1960) and has led to the following relation to predict the radius of the bubble,

$$\dot{r}_b = \frac{\kappa(T_0 - T_{\rm sat})}{h_{\rm lv}\rho_b\sqrt{\alpha t}}, \tag{17}$$

where α is the thermal diffusivity, $h_{\rm lv}$, the latent heat, κ, the thermal conductivity and t, the time.

Starting with a radius of 0.04 [mm], one can observe on Fig. 10, that the radius of a bubble at rest in a super-heated quiescent fluid, at 105 °C, computed iteratively using Eq. (6), agrees well with previous studies.

4. A problem and its parameterization

We consider water and vapor bubbles inside a cubical geometry of height h and width $h/2$. The bottom of the geometry (located at $y = 0$) is a wall (no-slip kinematic condition) maintained at temperature $T_{\rm hot}$. The sides are adiabatic walls. The top of the domain (located at $y = h$) is also walled and is maintained at temperature $T_{\rm cold}$, lower than $T_{\rm hot}$ and at atmospheric pressure. This corresponds to a classic Rayleigh–Bénard convection configuration for the liquid. Bubbles are injected at the lower base of the domain and are given an initial random position, an initial radius, $r_{b,0}$ and zero initial velocity. The total number of bubbles is considered constant. For this reason, when a bubble reaches the top of the geometry or collapses, it is taken out of the calculation and another bubble is re-injected at a random position, (x, z) at the bottom of the domain.

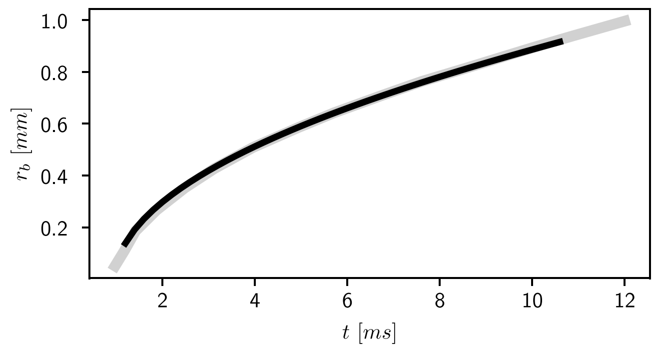

Fig. 10. Radius of a single bubble at rest in a quiescent fluid (black line) compared against the results obtained by Plesset and Zwick (1954) (grey line).

The reference temperature T_{ref} is defined as the mean between the top and bottom temperatures, $T_{\text{ref}} = (T_{\text{hot}} + T_{\text{cold}})/2$, while the reference temperature difference is defined as $\Delta T = T_{\text{hot}} - T_{\text{cold}}$.

Classical Rayleigh–Bénard convection is known to be governed by the Rayleigh and Prandtl numbers as well as the aspect ratio Γ. The addition of bubbles introduces several new phenomena. Thanks to their own buoyancy, the bubbles rise into the liquid, inducing movement and thermal mixing. The bubbles also absorb and release latent heat whenever they are in contact with either superheated ($T > T_{\text{sat}}$) or subcooled ($T < T_{\text{sat}}$) liquid. The phase change is driven by the efficiency of the heat transfer and the latent heat. This introduces a set of four additional parameters to characterize the flow under study, namely the number of bubbles over the domain, their initial size and two non-dimensional quantities related to the heat transfer process, namely the Jakob number and the degree of superheat.

The number of bubbles and their initial radius directly influence the bubble void fraction. However, for the same void fraction, more smaller bubbles or fewer bigger ones may be able to influence the flow differently. For this reason, we keep interest in both of these quantities.

The Jakob number scales the enthalpy difference of the liquid with respect to saturation with the latent heat. The latter takes two different definitions depending on the scale of interest; either the scale of a bubble or the scale of the whole flow. The bubble Jakob number, Ja_b, defined by Eq. (9), allows to parameterize the growth/collapse kinetics of each individual bubble. It is computed at each iteration and for each bubble present in the flow. It allows to compute the heat transfer coefficient, h_b and can be used to re-write the bubble radius equation, Eq. (6) to show its direct influence on bubble size variations,

$$\frac{\partial r_b}{\partial t} = \frac{h_b Ja_b}{\rho c_p}. \tag{18}$$

On the other hand, the global Jakob number, Ja allows for the parameterization of the flow as a whole. It is defined as the maximum Jakob number that any bubble may reach,

$$Ja = \frac{\rho c_p (T_{\text{hot}} - T_{\text{sat}})}{\rho_b h_{\text{lv}}}. \tag{19}$$

If its value is set to zero, corresponding to an infinite latent heat, bubbles can neither grow nor shrink. As it increases, bubbles are allowed to grow/shrink more and more. The global Jakob number is the one used as a governing parameter for the simulation.

The degree of superheat is defined as $\xi = \frac{T_{\text{hot}} - T_{\text{sat}}}{\Delta T}$ (Lakkaraju, 2012) and gives information about whether the liquid is mostly sub-cooled or superheated. The expression can be rewritten as $T_{\text{sat}} = (1-\xi)T_{\text{hot}} + \xi T_{\text{cold}}$, from which we can easily identify two trivial configurations. If $\xi = 0$, $T_{\text{sat}} = T_{\text{hot}}$, the liquid is fully sub-cooled, bubbles can only shrink. Whereas if $\xi = 1$, $T_{\text{sat}} = T_{\text{cold}}$, the liquid is fully superheated and bubbles will only grow. For any value in between 0 and 1, part of the fluid has a temperature above saturation, leading to bubble growth while the other part is sub-cooled and leads to the shrinkage of the bubbles. The degree of superheat allows to control the relative proportions of each part. One should note that a value of $\xi = 1/2$ leads to a reference temperature equal to the saturation one.

Table 1
Parameters fixed for this study: the Rayleigh number Ra, the Prandtl number Pr, the aspect ratio Γ, the degree of superheat ξ, the initial bubble radius $r_{b,0}$, the reference temperature T_{ref}, the reference thermal expansion coefficient β_{ref}, the height of the domain h and the temperature difference ΔT.

Ra	Pr	Γ	ξ	$r_{b,0}$ [μm]	T_{ref} [K]	β_{ref} [1/K]	h [cm]	ΔT [K]
2.12×10^5	1.75	1/2	1/2	12.5	373	$7.43e^{-4}$	1.79	0.25

Table 2
Cases description: the Jakob number Ja, the number of bubbles N_b, and the latent heat h_{lv}. Grid resolution criteria involve a number of cells $N_x \times N_y \times N_z$, the number of cells inside the hydrodynamic N_u, and thermal N_θ boundary layers, as well as the smallest $\frac{\Delta_{min}}{h}$ and the largest $\frac{\Delta_{max}}{h}$ cell sizes. The number in parentheses provide the minimum requirements according to Section 4.1.

Ja	N_b	h_{lv} [J/kg]	$N_x \times N_y \times N_z$	N_u	N_θ	$\frac{\Delta_{min}}{h}$ $\times 10^{-2}$	$\frac{\Delta_{max}}{h}$ $\times 10^{-2}$
Single phase			$50\times 70\times 50$	6 (3)	12 (6)	0.57	2.15 (6.74)
0	1000	∞	$50\times 70\times 50$	5 (2)	12 (5)	0.57	2.15 (7.94)
0.0001	1000	$8.49e^9$	$50\times 70\times 50$	5 (2)	12 (4)	0.57	2.15 (7.79)
0.001	1000	$8.49e^8$	$50\times 70\times 50$	2 (1)	12 (5)	0.57	2.15 (7.18)
0.01	1000	$8.49e^7$	$58\times 80\times 58$	3 (2)	10 (5)	0.50	1.88 (4.05)
0.05	1000	$1.70e^7$	$58\times 80\times 58$	1 (1)	7 (6)	0.50	1.88 (2.83)
0.1	1000	$8.49e^6$	$60\times 82\times 60$	1 (1)	6 (6)	0.43	1.92 (2.53)
0	2500	∞	$50\times 70\times 50$	3 (1)	11 (4)	0.57	2.15 (8.94)
0.0001	2500	$8.49e^9$	$50\times 70\times 50$	3 (1)	11 (4)	0.57	2.15 (8.31)
0.001	2500	$8.49e^8$	$50\times 70\times 50$	3 (2)	9 (5)	0.57	2.15 (6.03)
0.01	2500	$8.49e^7$	$50\times 70\times 50$	2 (2)	7 (5)	0.57	2.15 (3.33)
0.05	2500	$1.70e^7$	$58\times 80\times 58$	1 (1)	6 (6)	0.49	1.90 (2.32)
0.1*	2500	$8.49e^6$	$70\times 98\times 70$	1 (2)	6 (6)	0.36	1.61 (2.06)
0	5000	∞	$50\times 70\times 50$	3 (1)	9 (3)	0.57	2.15 (7.65)
0.0001	5000	$8.49e^9$	$50\times 70\times 50$	3 (1)	8 (3)	0.57	2.15 (7.16)
0.001	5000	$8.49e^8$	$50\times 70\times 50$	3 (2)	8 (4)	0.57	2.15 (5.16)
0.01	5000	$8.49e^7$	$50\times 70\times 50$	1 (1)	5 (5)	0.57	2.15 (2.78)
0.05	5000	$1.70e^7$	$88\times 124\times 88$	2 (2)	8 (6)	0.25	1.33 (2.03)
0.1*	5000	$8.49e^6$	$88\times 124\times 88$	1 (2)	7 (6)	0.25	1.33 (1.74)
0	10 000	∞	$50\times 70\times 50$	3 (1)	7 (3)	0.57	2.15 (6.44)
0.0001	10 000	$8.49e^9$	$50\times 70\times 50$	2 (1)	7 (3)	0.57	2.15 (6.12)
0.001	10 000	$8.49e^8$	$50\times 70\times 50$	4 (3)	6 (4)	0.57	2.15 (4.35)
0.01	10 000	$8.49e^7$	$58\times 80\times 58$	1 (1)	5 (5)	0.50	1.88 (2.36)
0.05*	10 000	$1.70e^7$	$88\times 124\times 88$	1 (2)	6 (6)	0.25	1.33 (1.78)
0.1*	10 000	$8.49e^6$	$88\times 124\times 88$	1 (2)	6 (6)	0.25	1.33 (1.49)

Within the framework of this paper, we focus on the influence of the Jakob number and the amount of bubbles on the flow. The Rayleigh and Prandtl numbers, the aspect ratio, the degree of superheat, the initial bubble radius and the reference temperature are fixed to the values given in Table 1. The Jakob number can be controlled in two different ways. The first way is to fix a height and a temperature difference that satisfy the values of Table 1 and to vary the latent heat to obtain the wanted Jakob number. The second option is to fix the latent heat to that of water at the reference temperature and to compute the temperature difference needed to obtain the desired Jakob value. The height of the domain is then calibrated to obtain the corresponding Rayleigh number. Whereas the second method is closer to reality, thanks to its h_{lv} value, the height and temperature difference would vary between two cases, leading to different void fractions if the number of bubbles and their sizes are not matched.

This paper offers an initial study that varies the Jakob number between 0 and 0.1 by adapting the latent heat. The height of the domain and the temperature difference used for these cases are given in Table 1. Various number of bubbles are investigated and the cases of interest are fully described in Table 2. Section 6 shows some results using the second method to drive the Jakob number and discusses how they compare to the first one.

4.1. Grid resolution

To ensure that the meshes used in our simulations are sufficiently refined to perform Direct Numerical Simulations (DNS), i.e, to resolve all the relevant scales of the flow (Pope, 2000), certain criteria must be met. These conditions can be broken down into two groups: the boundary layers and the bulk of the domain, where suitable limits are imposed respectively. A hyperbolic tangent expansion function is then used to gradually increase the cells dimensions from the wall towards the center

The first step is therefore to determine where the boundary layers end and the bulk starts. The thickness of both thermal and hydrodynamic boundary layers are therefore computed using either the location of the peaks in the time- and area-averaged RMS temperature and RMS horizontal velocity plots respectively or as the location of the intersection between bulk value and slope of the time- and area-averaged temperature and horizontal velocity profile near the boundaries respectively (Zhou and Xia, 2013). The above-mentioned profiles are obtained from data obtained by an initial, generally coarse, simulation. In our case, we computed the locations using both methods and kept the most restrictive condition.

Once the domain has been decomposed into bulk and boundary, one can apply the respective conditions to ensure a sufficiently refined mesh. The bulk criteria requires that cells have a maximum size given by,

$$\frac{2max(\eta_B|y)}{l_{ref}} \quad \text{for } Pr > 1 \qquad \text{and} \qquad \frac{\pi min(\eta_K|_{bulk})}{l_{ref}} \quad \text{for } Pr \leq 1 \tag{20}$$

where the Kolmogorov length scale, η_K and the Bachelor length scale, η_B are respectively obtained as a function of the energy dissipation rate ϵ_u (Shishkina et al., 2010; Grötzbach, 1983),

$$\eta_K = \left(\frac{\nu^3}{\epsilon_u}\right)^{\frac{1}{4}}, \quad \eta_B = \left(\frac{\nu\kappa^2}{\epsilon_u}\right)^{\frac{1}{4}} = \eta_K Pr^{-\frac{1}{2}}, \quad \epsilon_u = \frac{\nu}{2}\sum_i\sum_j\left(\frac{\partial u_i}{\partial x_j} + \frac{\partial u_j}{\partial x_i}\right)^2. \tag{21}$$

The theoretical minimum number of cells required in the kinetic, N_u and thermal, N_θ boundary layers are obtained respectively as Shishkina et al. (2010)

$$\left.\begin{aligned} N_u &= 2^{\frac{1}{2}} a Nu^{\frac{1}{2}} Pr^{\frac{1}{3}} E^{\frac{3}{2}} \\ N_\theta &= 2^{\frac{1}{2}} a Nu^{\frac{1}{2}} E^{\frac{3}{2}} \end{aligned}\right\} \quad \text{for } Pr > 3, \tag{22}$$

$$\left.\begin{aligned} N_u &= 2^{\frac{1}{2}} a Nu^{\frac{1}{2}} Pr^{(-0.0355+0.033 log(Pr))} \\ N_\theta &= 2^{\frac{1}{2}} a Nu^{\frac{1}{2}} Pr^{(0.03215+0.011 log(Pr))} \end{aligned}\right\} \quad \text{for } Pr \leq 3,$$

with $a = 0.482$ and $E = 0.982$. Estimations of the energy dissipation rate and the Nusselt number are once again computed from the previously obtained data. The number of cells for a given expansion factor β are finally computed to obtain the final, optimally refined mesh. Table 2 details the number of cells used in each simulation. It also gives the actual number of cells in the two boundary layers and compares it with the figure in brackets representing the theoretical value obtained from Eqs. (22). Lastly, Table 2 gives the values of the smallest and largest cells and compares them with the theoretical limit, obtained using Eqs. (20), in parenthesis.

It can be seen from Table 2 that several cases with high Jakob numbers do not meet the said conditions for the kinetic boundary layer (these are highlighted with a $*$ symbol). Indeed, the higher the Jakob number, the larger the bubbles and the higher their velocities, which does not appear to be numerically compatible with smaller cells. As the DNS aspect was initially only applied to the liquid phase of the problem, and the meshes were improved as much as possible, we decided to analyze these results anyway.

5. Results

To familiarize ourselves with the complex multiphase flow studied in this paper, the following sections present and discuss the flow topology, bubble-related statistics, Nusselt number and turbulence statistics for various Jakob numbers and amounts of bubbles. For purposes of non-dimensionalization, the height h, free-fall velocity $u_{\mathrm{ff}} = \sqrt{\beta_{\mathrm{ref}} g h \Delta T}$ (where β_{ref} is the thermal expansion coefficient at the reference temperature T_{ref} and is given in Table 1) and free-fall time $t_{\mathrm{ff}} = h/u_{\mathrm{ff}}$ are used as the reference length, velocity and time unit, respectively. The obtained non-dimensional fields are indicated with a hat ˆ symbol. It is noted that the time average of a generic quantity ψ is denoted by $\langle\psi\rangle_t$, the time- and area-average (i.e. across horizontal planes) by $\langle\psi\rangle_{txz}$ and the time- and volume-averaged by $\langle\psi\rangle_{txyz}$. For bubble-related fields, the average of a generic field ψ_b over the bubble population is denoted by $\langle\psi_b\rangle_b$.

5.1. Convective structures of the flow

The classical Rayleigh–Bénard convection flow (single phase) in a cubic geometry consists of a Large-Scale Circulation (LSC) aligned with a diagonal, called the primary plane, and of four counter-rotating vortices in the secondary (also called orthogonal) diagonal plane. Fig. 11a and b display the time-averaged streamlines of such a flow while Fig. 11c and d present contour plots of the mean amplitude of the in-plane velocity component superposed with the in-plane velocity vectors at the primary and secondary diagonal planes respectively. The LSC is the main structure of the flow and results from the creation of hot and cold plumes emerging from the lower and upper boundary layers respectively. Hot plumes rise near a corner of the geometry while cold ones sink along the opposite one, thereby leading to the formation of impingement points, i.e. points where the hot/cold 'columns' of fluid collide on the upper/lower surfaces. The orthogonal plane (Fig. 11d) contains counter-rotating vortices, interacting with one another at mid-height and mid-length. The flow is therefore symmetrical along the diagonal axis containing the LSC.

The addition of bubbles to the flow affects the structure of the liquid phase via the two-way coupling. Figs. 12 and 13 as well as Figs. 14 and 15 illustrate these structure modifications for various Jakob numbers with 1000 and 10 000 bubbles respectively. In the cases with 1000 bubbles and low Jakob numbers, $Ja = 0$ and 0.0001, (Figs. 12 and 13 (a–b)) the flow structure is similar to classical RBC. The highest fluid velocities, however, are lower than in the single-phase problem. Moreover, the presence of bubbles leads to the appearance of asymmetries in the flow. The ascending plume (on the left corner of Fig. 12 (a–b)), which extended from one corner to the diagonal in the single-phase case, now extends beyond the diagonal. The separation between ascending and descending fluid is now an arc rather than the diagonal. In addition, the secondary planes (bottom plots on Fig. 13 (a–b)) feature a full-height convection cell and two vortices. The convection cell can be seen as the fusion of two of the four counter-rotating vortices present in the single-phase case (see Fig. 11d), while the other two tend to fade away.

As the 1000 vapor bubbles are allowed to grow/shrink when the Jakob number is increased, the flow is greatly affected, switching from the previously described "single diagonally oriented roll" structure to a "nearly toroïdal roll" structure according to Pallarès et al. (2001). The emissions of volumes of hot fluid from the lower boundary, i.e. "hot plumes", rise along the four corners of the geometry while the cold ones sink in the middle. In Fig. 13 (d–e), we can therefore observe the presence of four convection cells, some of them more prominent. The flow becomes symmetrical and the primary and secondary planes become similar/interchangeable. A similar structural change in the presence of bubbles was observed by Oresta et al. (2009), but in a cylinder at substantially higher Jakob numbers. Furthermore, this transition from "single diagonally oriented roll" to a "nearly toroïdal roll" structure,

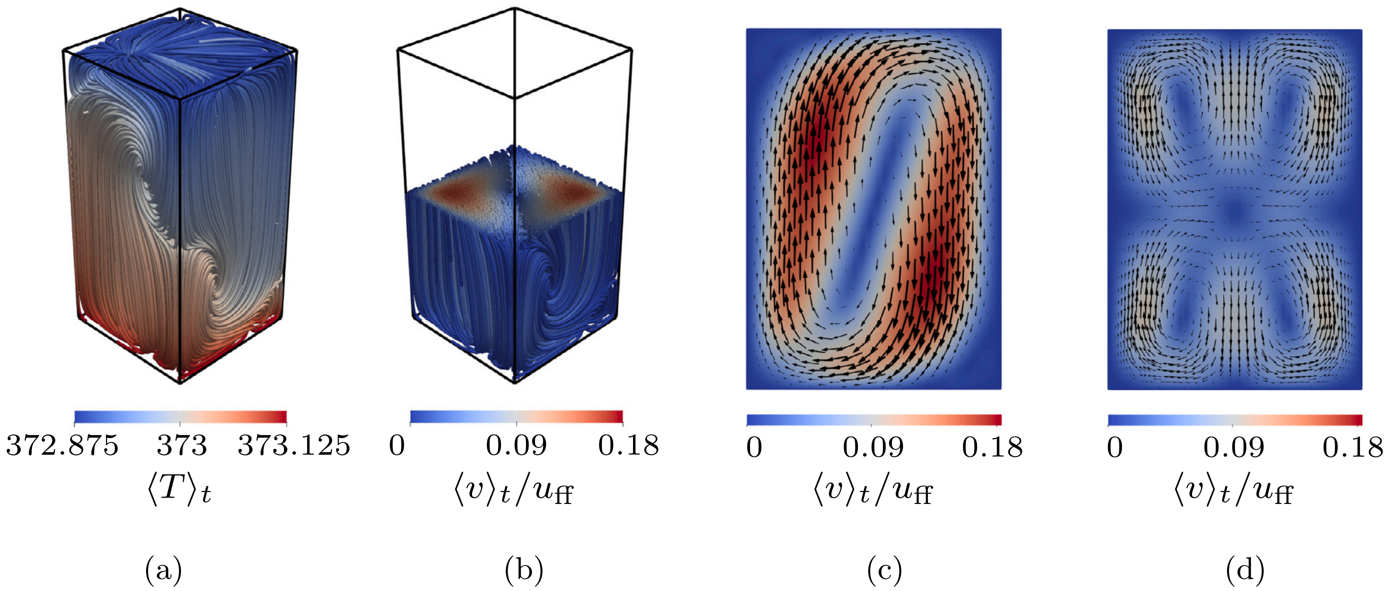

Fig. 11. Single phase case. Time-averaged streamlines (a) colored with temperature, (b) clipped at mid-height with a velocity magnitude coloring. Contour plots of the mean magnitude of the in-plane vertical velocity, $\langle v\rangle_t$, with superposed in-plane velocity vectors at (c) the primary and (d) the orthogonal planes. (For interpretation of the references to color in this figure legend, the reader is referred to the web version of this article.)

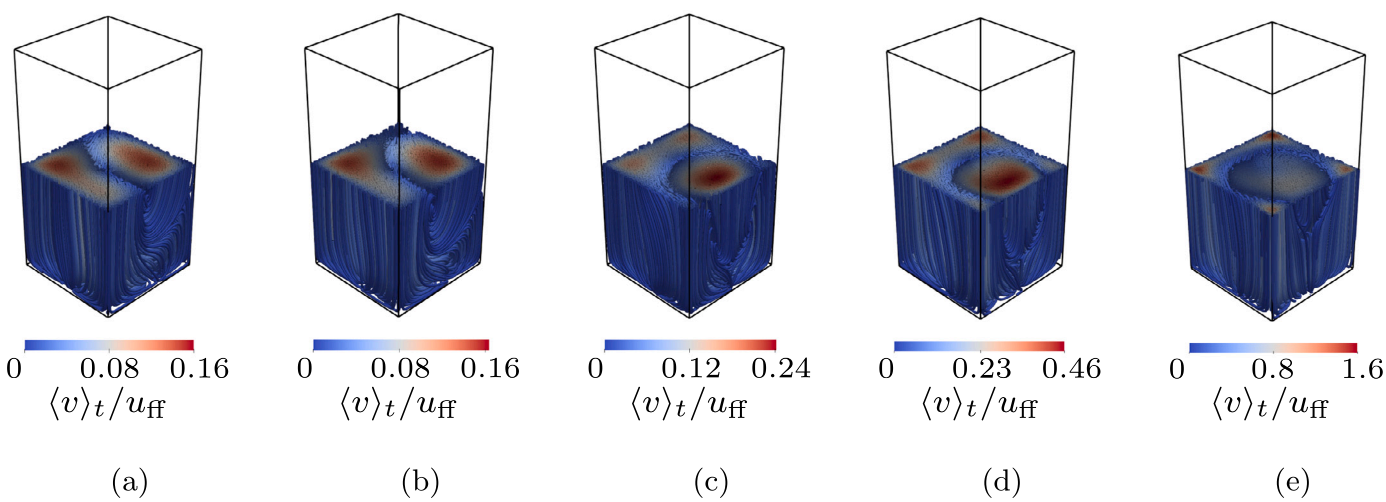

Fig. 12. Time-averaged streamlines clipped at mid-height with a velocity coloring for 1000 vapor bubbles. (a) $Ja = 0$ (b) $Ja = 0.0001$ (c) $Ja = 0.001$ (d) $Ja = 0.01$ (e) $Ja = 0.1$. (For interpretation of the references to color in this figure legend, the reader is referred to the web version of this article.)

involving the division of the LSC into two convective cells and the fusion of two counter-rotating vortices, seems to bear similarities to the phenomenon of LSC reorientations in classical Rayleigh–Bénard convection which is described by Vishnu et al. (2020).

When 10 000 bubbles are introduced into the flow (Figs. 14 and 15), a “nearly toroïdal roll” structure is always observed, whatever the Jakob number. The Jakob number, on the other hand, appears to impact the relative size of ascending plumes (located in the four corners) versus descending plumes (located in the center of the domain). As bubbles are given more freedom to grow/shrink, the downward flow expands, pushing the four upward flows into the corners and for some values of Jakob number leading to asymmetries. Indeed, the descending plume, which sinks into a circle in the middle of the domain and is initially centered for $Ja = 0$, gradually decenters towards one of the sides while some of the four ascending plumes grow larger than others. As the Jakob number grows large enough, the symmetry appears to be recovered.

The distribution of bubbles within the domain is consistent with the flows observed previously as illustrated by Figs. 16 and 17, which show the instantaneous distribution of bubbles colored by radius size and the time-averaged bubble volume fraction on different horizontal planes for 1000 and 10 000 bubbles respectively. For $Ja = 0$, bubbles occupy the whole space; they cannot grow/shrink and therefore rise towards the upper surface. The bubble void fraction is similar at all heights. When bubbles are allowed to grow/shrink, four columns of bubbles, located near the corners, form and predominate. Bubbles initially in the center of the domain either join one of the columns or collapse. The higher up, the more concentrated the bubbles are in the corners.

The most intriguing aspect of this flow topology analysis is the change in flow structure. The latter does not occur for all flows containing bubbles, but seems to depend on the quantity and properties of these bubbles. In order to better figure out the phenomenon, Fig. 18 displays the time- and volume-averaged bubble void fraction, $\langle\phi_b\rangle_{txyz}$ as a function of the number of bubbles, N, for various cases. “Single diagonally oriented roll” structures are represented by circles, while “nearly

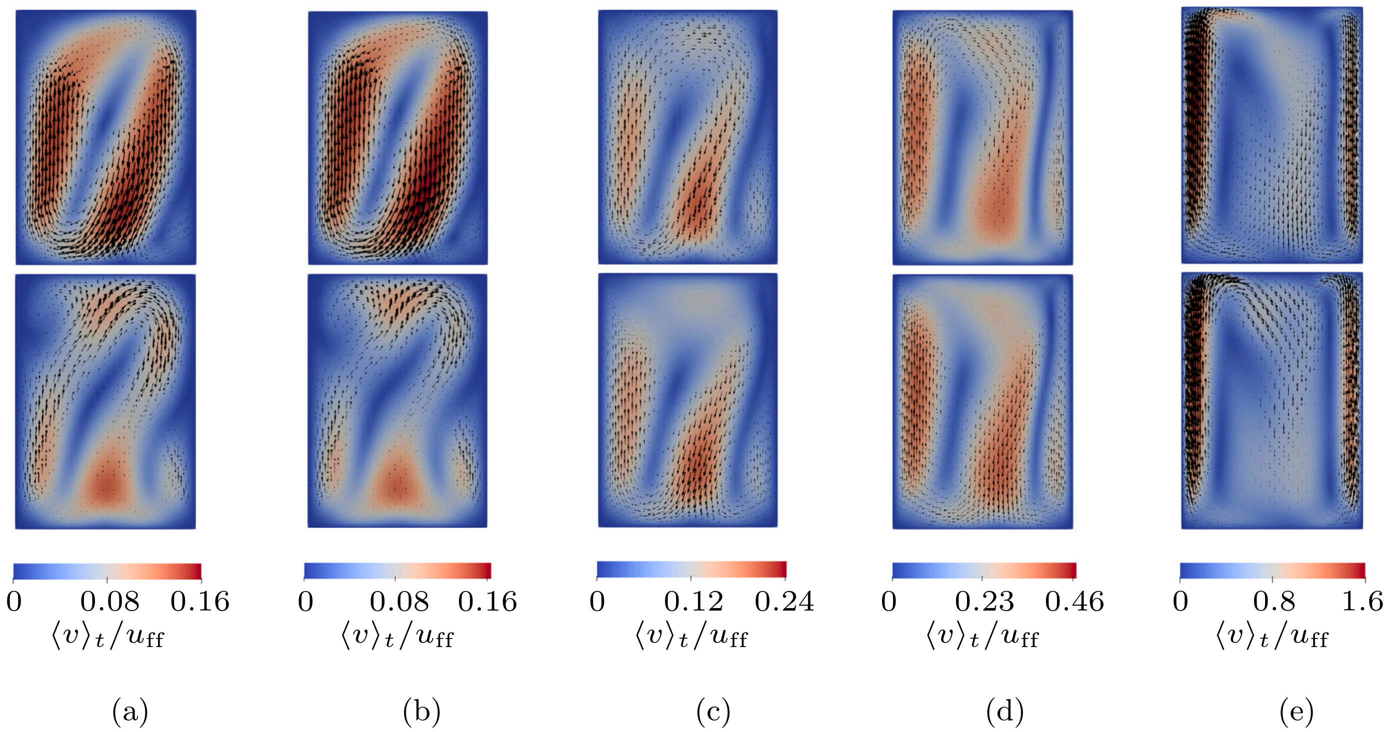

Fig. 13. Contour plots of the mean amplitude of the in-plane velocity component, $\langle v\rangle_t$, with superposed in-plane velocity vectors at the primary (top) and secondary (bottom) diagonal planes for 1000 vapor bubbles.(a) $Ja = 0$ (b) $Ja = 0.0001$ (c) $Ja = 0.001$ (d) $Ja = 0.01$ (e) $Ja = 0.1$. (For interpretation of the references to color in this figure legend, the reader is referred to the web version of this article.)

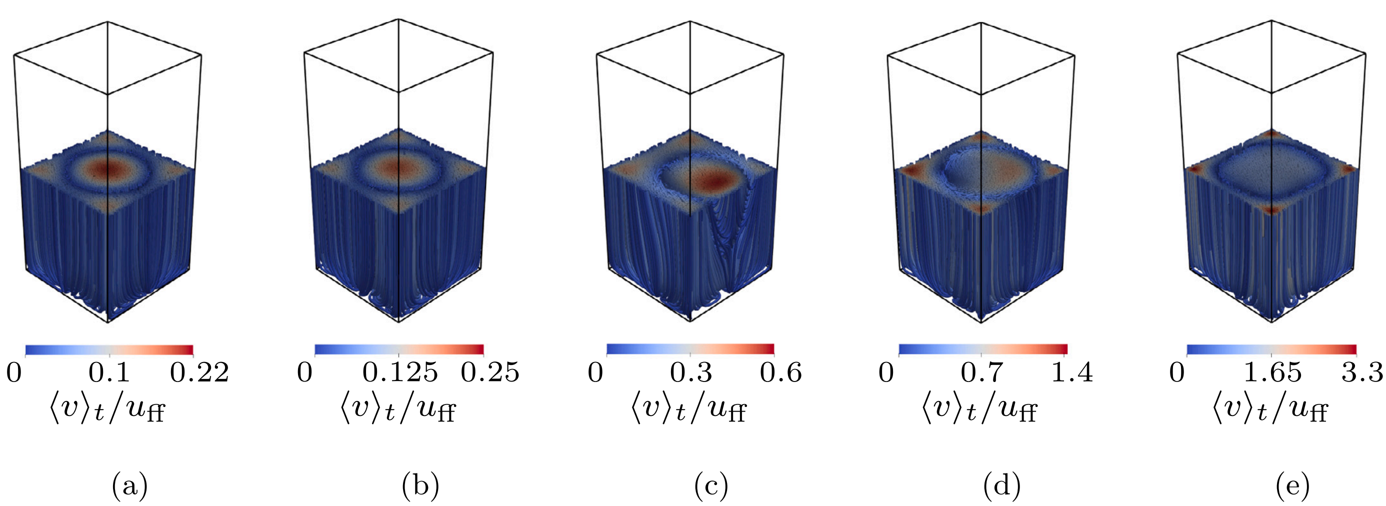

Fig. 14. Time-averaged streamlines clipped at mid-height with a velocity coloring for 10 000 vapor bubbles. (a) $Ja = 0$ (b) $Ja = 0.0001$ (c) $Ja = 0.001$ (d) $Ja = 0.01$ (e) $Ja = 0.1$. (For interpretation of the references to color in this figure legend, the reader is referred to the web version of this article.)

toroïdal roll'' structures are represented by triangles. The structures are identified both by checking the 3D streamlines and the velocities at the center of the domains. Indeed, high downward velocities indicate a ``nearly toroïdal roll'' structure, while lower downward velocities indicate the other structure. The limit between the two is found to be at $v/u_{\rm ff} \approx -0.07$ for the cases investigated herein. The figure contains the cases described in Table 2 in color. The different colors refer to the value of the Jakob number, while shading is low for small quantities of bubbles and increases for larger amounts. This approach is also used in the rest of this section. Additional cases are added to complete the analysis. These are shown in gray and all have a Jakob number equals to zero while bubble radii have been modified to obtain the desired bubble volume fraction (see Appendix A for more details). One can observe on Fig. 18 that the structure appears to be directly linked to the bubble void fraction. In a way, a certain threshold (which ranges in the gray zone on Fig. 18) must be reached for the classic LSC to give way to the toroïdal structure. Although this is true in general, we note that for the same volume fraction (close to the ``threshold''), fewer large bubbles or more small bubbles can lead to different structures. The phenomenon is therefore based on the overall bubble volume fraction and, more subtly, on the way in which it is achieved, i.e. the number of bubbles and their sizes.

This section has highlighted and described the two structures that the flow can take on, namely a typical RBC structure with a LSC or

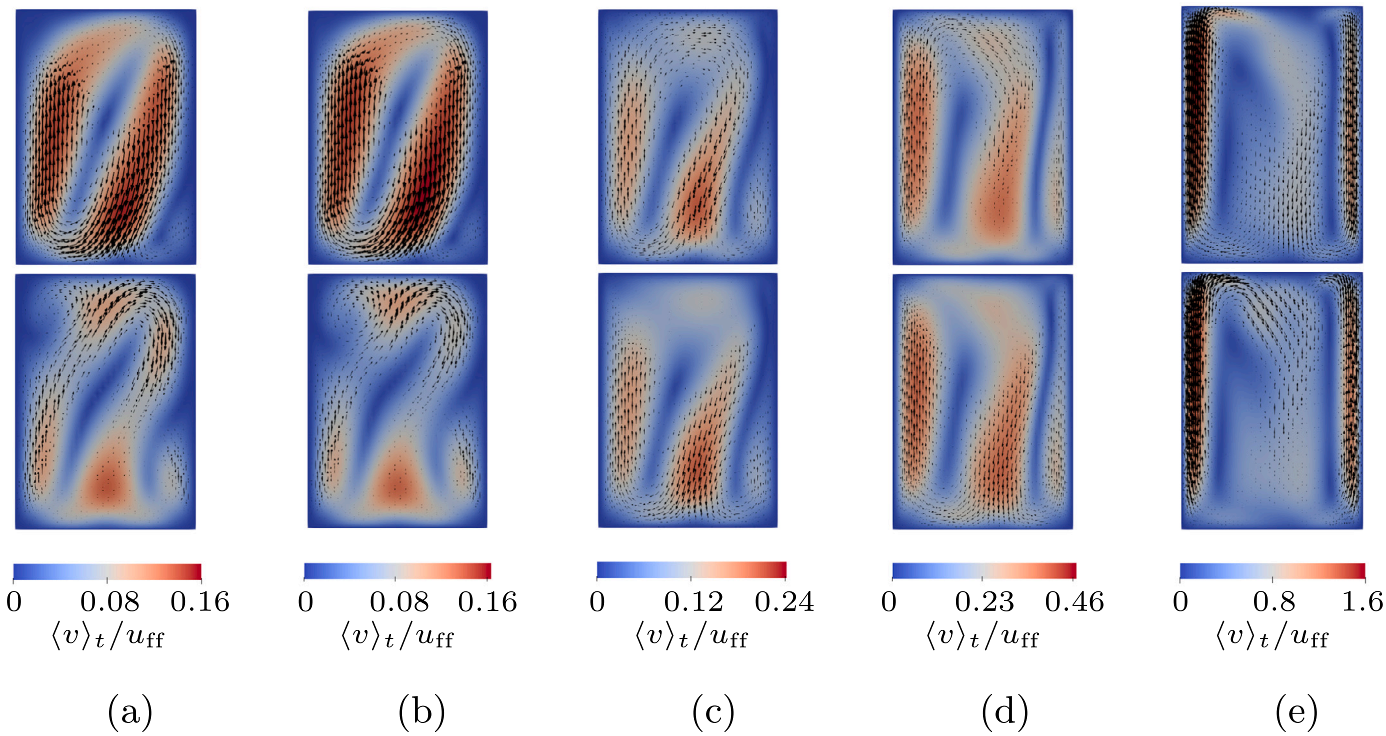

Fig. 15. Contour plots of the mean amplitude of the in-plane velocity component, $\langle v\rangle_t$, with superposed in-plane velocity vectors at the primary (top) and secondary (bottom) diagonal planes for 10 000 vapor bubbles.(a) $Ja = 0$ (b) $Ja = 0.0001$ (c) $Ja = 0.001$ (d) $Ja = 0.01$ (e) $Ja = 0.1$. (For interpretation of the references to color in this figure legend, the reader is referred to the web version of this article.)

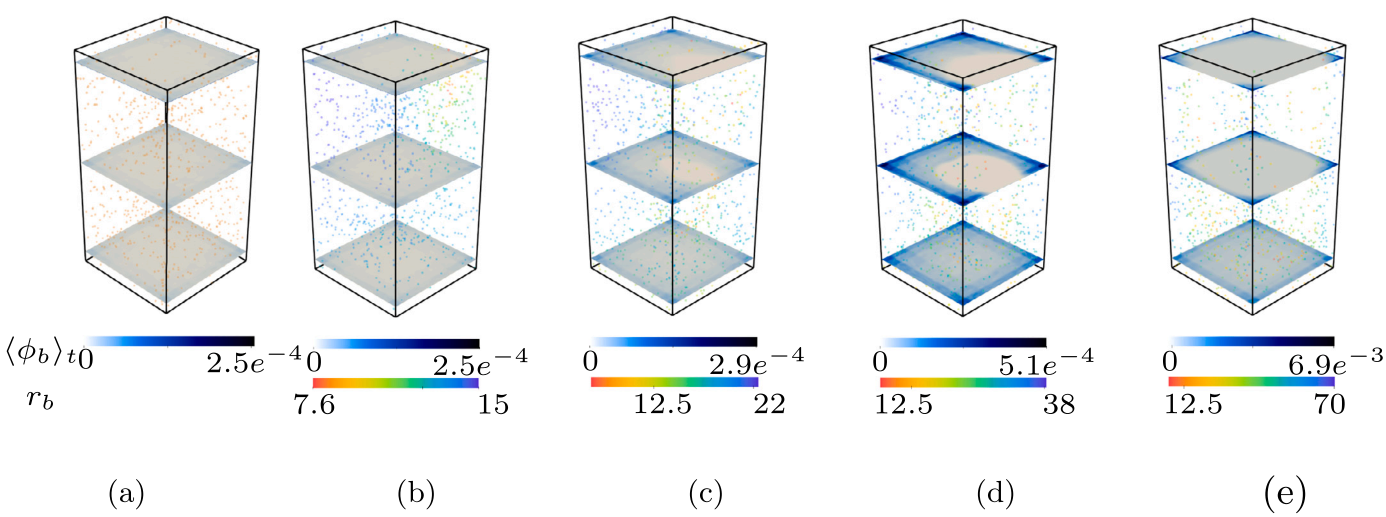

Fig. 16. Time-averaged bubble void fraction $\langle \phi_b\rangle_t$ at horizontal planes located at 5, 50 and 95% of the domain height, superimposed with the instantaneous bubble distribution (at time $t = 200\ t_{ff}$) colored with radius (in μm) for 1000 vapor bubbles. (a) $Ja = 0$ (b) $Ja = 0.0001$ (c) $Ja = 0.001$ (d) $Ja = 0.01$ (e) $Ja = 0.1$. (For interpretation of the references to color in this figure legend, the reader is referred to the web version of this article.)

a "nearly toroidal roll" with rising fluid in the four corners of the geometry. In both cases, the variation in Jakob number has various effects on the flow, such as asymmetries and more or less intense velocities. At first glance, the structure seems to be determined by the void fraction of the bubbles. On closer inspection, however, it becomes clear that this depends more specifically on the number of bubbles and their size. The following sections will provide a more quantitative analysis of the flow, enabling us to better understand the structures described here.

5.2. Bubble related statistics

As the Jakob number increases, the mean bubble radius follows a square-root curve as displayed by Fig. 19a. For smaller amounts of bubbles, radii tend to be higher. Indeed, the more bubbles there are, the more energy is exchanged between the two phases via the coupling term f_T. This leads to a better thermodynamic equilibrium between the bubbles and the liquid, limiting bubble growth or shrinkage. These

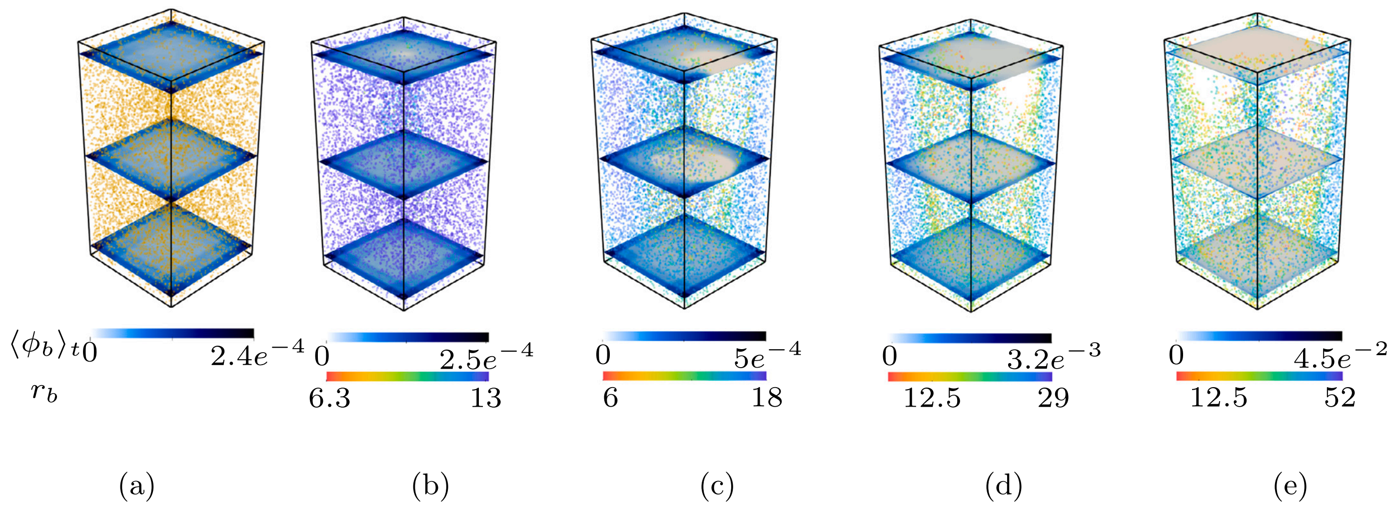

Fig. 17. Time-averaged bubble void fraction $\langle \phi_b \rangle_t$ at horizontal planes located at 5, 50 and 95% of the domain height, superimposed with the instantaneous bubble distribution (at time $t = 200\ t_{ff}$) colored with radius (in µm) for 10 000 vapor bubbles. (a) $Ja = 0$ (b) $Ja = 0.0001$ (c) $Ja = 0.001$ (d) $Ja = 0.01$ (e) $Ja = 0.1$. (For interpretation of the references to color in this figure legend, the reader is referred to the web version of this article.)

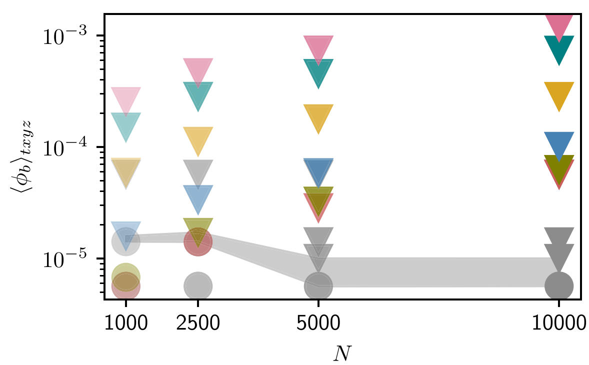

Fig. 18. Time and area-averaged bubble void fraction, $\langle \phi_b \rangle_{txyz}$ as a function of the number of bubbles, for the cases of Table 2: $Ja = 0$ (▼), $Ja = 0.0001$ (▼), $Ja = 0.001$ (▼), $Ja = 0.01$ (▼), $Ja = 0.05$ (▼) and $Ja = 0.1$ (▼) as well as additional cases at $Ja = 0$ (▼). "Single diagonally oriented roll" structures are identified with circles (●) while "nearly toroïdal roll" structures are represented with triangles (▼). The postulated boundary between the two types of structure is highlighted (▬).

energy exchanges between the two phases will be analyzed in greater detail in the following sections.

Fig. 19b displays the probability density function of the radius. As the Jakob number is increased, the mean value also increases, which is in line with what was observed before. However, the graph also shows a significant increase in standard deviation, meaning that bubble radii cover a wider range of values and the maximum value reached is increasingly greater. Similarly as for Fig. 19a, less bubbles lead to higher radii.

The time and volume averaged bubble fraction, $\langle \phi_b \rangle_{txyz}$ is plotted for all cases understudy in Fig. 20. Although an increase of bubble number led to smaller mean radii (see Fig. 19a), the total volume occupied by bubbles increases with the addition of bubbles. To take the analysis a step further, the bubble void fraction is broken down into four components based on the properties of the surrounding fluid, i.e. rising/descending and hot/cold (as compared to the saturation temperature). Fig. 20 shows that most of the vapor phase is located in the ascending plumes, both hot and cold. This is all the more true as the Jakob number increases. Indeed, at high Jakob number, the vapor phase is almost non-existent in the descending plumes.

Elghobashi (1994) has developed a mapping system that links bubble volume fractions to the necessary coupling models. According to this classification map, two-way coupling, without accounting for bubble-bubble interactions, can be safely used for bubble volume fractions up to 10^{-3}. Our global values are therefore in an acceptable range for two-way coupling. However, as shown in Figs. 16 and 17, locally the bubble void fraction can take much higher values, necessitating consideration of bubble-bubble interactions. For the purposes of this paper, we restrict ourselves to two-way coupling only, although we are aware that we are reaching the limits of the model.

5.3. Nusselt number and convection intensity

As vapor bubbles are known to enhance heat transfer, this section focuses on identifying and quantifying the various mechanisms involved. The mean vertical heat flux passing through the domain is measured by the local Nusselt number and is derived by integrating the energy equation in time and over the horizontal directions. The latter presents an additional term as compared to classical Rayleigh–Bénard convection. Indeed, the effect of bubbles on the fluid leads to an additional term in the energy equation, thereby leading to a third term in the expression of the Nusselt number. The local Nusselt number through each horizontal plane of the domain at various vertical locations is therefore expressed as,

$$\langle Nu \rangle_y \ = \underbrace{\sqrt{RaPr}\langle \hat{\rho}\hat{c}_p \hat{u}\hat{T} \rangle_{txz}}_{Convection} \underbrace{-\langle \hat{\kappa}\frac{\partial \hat{T}}{\partial \hat{y}} \rangle_{txz}}_{Diffusion} \underbrace{- \int_0^{\hat{y}} \langle \hat{f}_T \rangle_{xzt} dy}_{Bubbles} . \tag{23}$$

The global or volume-averaged Nusselt number, Nu is obtained by averaging one more time in the vertical direction. The full derivation of this expression can be found in Appendix B. Fig. 21 shows the global Nusselt number and its breakdown into the three possible components for various values of Jakob number and number of bubbles. Generally, the Nusselt increases with the Jakob number and with the number of bubbles.

Out of the three components composing this flux, i.e. diffusion, bubbles and convection, only two vary with the Jakob number and/or amount of bubbles. Indeed, the diffusion term appears to be independent of the vapor phase. The bubble-related flux, which is directly linked to the energy additional term f_T, can be seen as the energy that is acquired by the bubbles as they grow and which is then transported by the bubbles across the domain. Since f_T, see Eq. (14), depends directly on the number of bubbles but also on the size of their surface

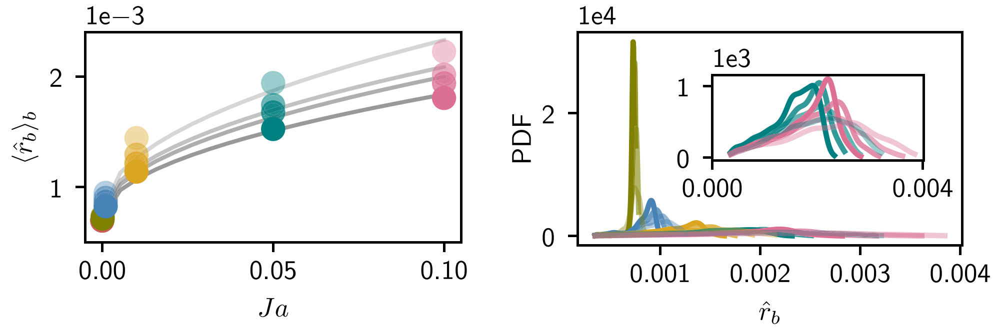

(a) (b)

Fig. 19. (a) Mean normalized bubble radius, $\langle \hat{r}_b \rangle_b$ and (b) probability density function of the bubbles radii after 200 t_{ff} for $Ja = 0$ ( ), $Ja = 0.0001$ ( ), $Ja = 0.001$ ( ), $Ja = 0.01$ ( ), $Ja = 0.05$ ( ), $Ja = 0.1$ ( ) and 1000, 2500, 5000 and 10 000 bubbles from lightest to darkest shades. Fits of the data of the type: $\langle \hat{r}_b \rangle_b = a + b\sqrt{Ja}$ are added in gray.

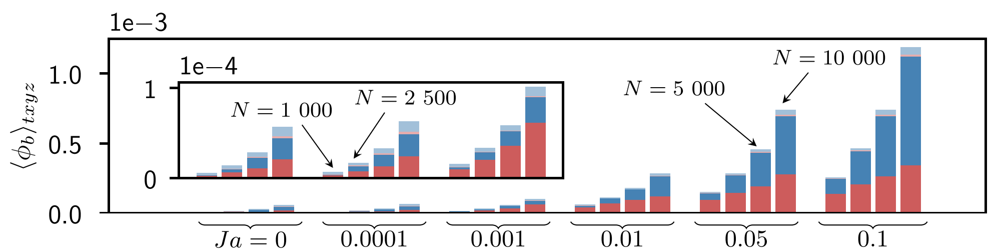

Fig. 20. Time and volume-averaged bubble void fraction for Jakob numbers ranging from 0 to 0.1 and containing 1000, 2500, 5000 or 10 000 bubbles. The field has been filtered according to the properties of the surrounding liquid either rising and hot ($T > T_{sat}$) ( ), rising and cold ($T < T_{sat}$) ( ), sinking and hot ( ) or sinking and cold ( ).

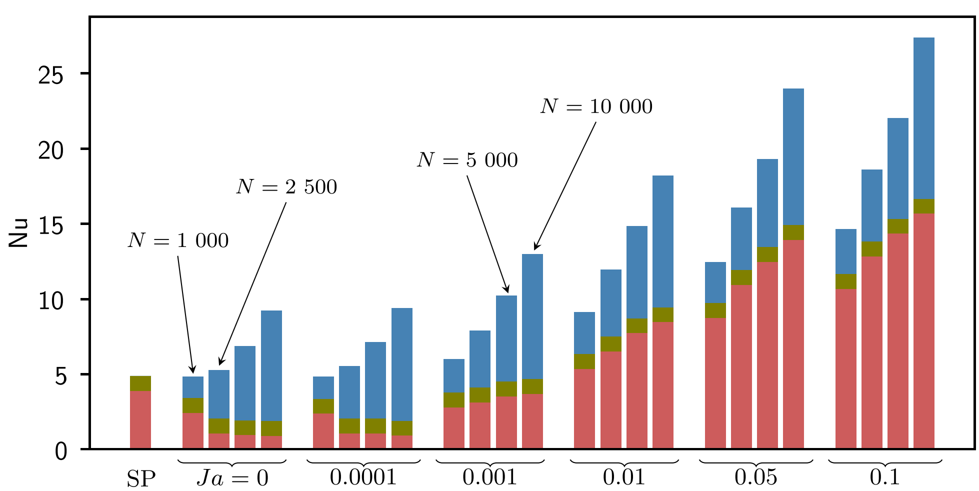

Fig. 21. Nusselt number for simulations at $Ra = 2.12 \times 10^5$ with Jakob numbers ranging from 0 to 0.1 and containing 1000, 2500, 5000 or 10 000 bubbles. Convection ( ), diffusion ( ) and bubble-related ( ) components of the volume-averaged Nusselt number.

($4\pi r_b^2$), we observe that this flux increases strongly with the number of bubbles present but also slightly with increasing Jakob number. Fig. 22(b), to be analyzed shortly, will once again highlight these influences. Finally, the convection term is decreased when the Jakob number is low ($Ja \leq 0.0001$), regardless of the number of bubbles. As the Jakob number increases ($Ja > 0.0001$), the convection component begins to rise with both the Jakob number and the number of bubbles.

In order to better understand these trend changes in terms of convection, one must analyze the coupling between the two phases. The bubbles affect the liquid phase through additional terms in the momentum and energy equations, $\boldsymbol{f}_u$ and f_T respectively. The first one, the momentum source term, represents an additional bubble-induced forcing due to the fact that bubbles with their low density have a tendency of rising. It is a mechanical forcing term for the liquid. It is generally positive, as the bubbles tend to rise, but it can either promote or oppose fluid movement if the surrounding fluid is either rising or sinking. On the other hand, the thermal source term comes from the fact that bubbles tend to absorb/evacuate heat if the surrounding fluid's temperature is greater/lower than the saturation one, therefore lessening the temperature gradients and hindering the natural convection of the liquid. This thermal effect has already enabled us to explain why the average bubble radius is smaller for a higher number of bubbles (see Fig. 19a).

Figs. 22(a) and 22(b) display the time and volume-averaged momentum (in the vertical direction) and thermal source terms respectively. Only their trends should be compared together, as they do not have the same units and are therefore not comparable. Each term has been broken down into two components. For the momentum one, the first component contains the values averaged over the locations where the fluid rises and the second where it falls. On the other hand, the energy source term is broken down according to the surrounding fluid temperature, either hot ($T > T_{\mathrm{sat}}$) or cold ($T < T_{\mathrm{sat}}$). In the following paragraphs, we first examine the momentum source term, then the thermal source term, and finally combine them to understand the overall effect on the flow.

The momentum source term, Fig. 22(a), is created almost exclusively in the rising fluid and is therefore an overall aid to the liquid upward circulation; it can be seen as a mechanical effect of the bubbles on the fluid. The values appear to be directly related to the bubble volume fraction, $\langle \phi_b \rangle_{txyz}$ (Fig. 20) and are therefore very low for low Jakob numbers, but increase sharply and unrestrictedly as the Jakob number and the number of bubbles increase.

The energy source term, Fig. 22(b), shows very small net values (highlighted by black frames) at low Jakob numbers ($Ja \leq 0.0001$) and increased ones at higher Jakob numbers, explaining among other things, the bubble-related flux trends discussed previously. Breaking down the term provides additional information. At low Jakob number, the bubbles are everywhere, the thermal effect tends to reduce temperature gradients on both the hot ($f_T < 0$) and the cold ($f_T > 0$) sides, so the temperatures around the bubbles converge towards the saturation temperature, resulting in a net effect of f_T, on the total volume, of almost zero. As the Jakob number increases, bubbles are concentrated in the rising streams of fluid located in the corners (see Fig. 20). The thermal source term therefore also has the effect of reducing temperature gradients, but the effect is more intense on the hot side. This asymmetry between hot and cold impacts turbulence statistics, as will be discussed in Section 5.4. In all cases, i.e. for low and high Jakob numbers, the effect of f_T is to reduce temperature gradients within the liquid and therefore convection driven by buoyancy.

The liquid circulation is therefore mechanically favored by the momentum source term, and increasingly so as Jakob and bubble numbers increase. Convection is also penalized by the thermal term. However, this penalty is limited by the temperature spectrum: once the gradients are completely reduced, the effect is at its maximum. The combination of both these effects results in a very low convection-related Nusselt number at low Jakob number, and we can even say that a lower ceiling seems to be reached. As the Jakob number increases, the thermal effect is limited as explained beforehand, while the momentum effect continues to increase, resulting in an increase in convection which is all the higher the greater the Jakob number and amount of bubbles.

In general, the Nusselt number is enhanced with the presence of bubbles. When bubbles cannot/almost cannot grow (low Ja), the improvement is due solely to the heat transported by bubbles while the liquid phase faces a decrease in buoyancy-convection. As the bubbles expand and collapse more freely, the Nusselt number increases across all its components: convection, diffusion and bubbles. For the cases investigated herein, i.e. Rayleigh numbers of 2.12×10^5, the maximum Nusselt number reached (10 000 bubbles and $Ja = 0.1$), is 5 times greater than the single-phase case. The value reached by the latter case is equivalent to a single phase case at a Rayleigh number of 3.26×10^7, according to the correlation of Niemela et al. (2000).

5.4. Turbulence statistics

The last results studied in this analysis concern the turbulence statistics related to the liquid phase, which can be obtained thanks to the DNS approach chosen for this phase. These results are typical for Rayleigh–Bénard convection (Zhou and Xia, 2013; Hay and Papalexandris, 2019; Kerr, 1996) and they allow to compare the flow understudy to classical single-phase RBC trends.

In Fig. 23a and b, we present plots of the mean normalized temperature, $\langle \theta \rangle_{txz}$ for various amounts of bubbles and $Ja = 0$ and 0.1 respectively. At $Ja = 0$, the temperature values in the bulk of the domain tend towards a homogeneous value. This phenomenon is accentuated when the number of bubbles is higher, and illustrates the impact of the additional energy term, f_T on the flow (see Fig. 22(b)), which causes temperature gradients within the domain to disappear. At high Jakob numbers ($Ja = 0.1$), the profiles also tend to standardized, but around a temperature below that of saturation. In fact, the energy source term has a greater impact on the hot part of the flow than on the cold part (see Fig. 22(b)). The hot part therefore cools more than the cold part warms, leading to lower temperatures when surface averages are applied. The s-shape profile of the single phase problem is due to the fact that the Rayleigh number is very low, $Ra = 2.12 \times 10^5$ and therefore at the limit between the laminar and turbulent regimes.

Fig. 23c and d display the RMS of the normalized temperature profiles, $\theta_{\mathrm{RMS}} = \sqrt{\langle \theta^2 \rangle_{txz} - \langle \theta \rangle_{txz}^2}$ for different number of bubbles and $Ja = 0$ and 0.1 respectively. In all cases, the shape of the profiles, i.e. peaks at the end of the boundary layers and smaller values in the bulk, are identical to single-phase thermal convection. In both cases, the values in the bulk tend to decrease with increasing amounts of bubbles. This trend is analogous to that for an increase in the Rayleigh number (Hay and Papalexandris, 2019), which is explained by higher turbulence intensities resulting in more efficient thermal mixing. In our cases, the better thermal mixing is obtained thanks to the bubbles. One may also note that values at $Ja = 0$ are lower than the ones for $Ja = 0.1$. Indeed, as the bubbles are uniformly distributed at $Ja = 0$ and clustered in the corners at $Ja = 0.1$, they enable better thermal mixing in the former case.

Vertical and horizontal velocity RMS profiles are displayed in Fig. 24. The RMS of the vertical velocity component, v_{RMS}, exhibits a "parabolic-like" profile with null values at the upper and lower boundaries. The RMS of the horizontal velocity component is obtained as, $u_{\mathrm{RMS}} = \sqrt{\langle u^2 \rangle_{txz} - \langle u \rangle_{txz}^2 + \langle w^2 \rangle_{txz} - \langle w \rangle_{txz}^2}$ and the profiles present local peaks near the boundaries, signaling the edge of the hydrodynamic boundary layers (Kerr, 1996). At high Jakob number, both the vertical and horizontal profiles display higher values than the single phase case, illustrating an increase in turbulence intensity, which is further enhanced with greater amounts of bubbles. This evolution is similar to what would have been obtained for single phase cases with increasing Rayleigh number (Hay and Papalexandris, 2019; Kerr, 1996). At low Jakob number, the opposite trend can be observed. Values are lower than in the single-phase case, depicting a decrease in turbulence.

At Jakob number higher than 0.0001, any increase of the Jakob number itself or in the number of bubbles leads to an evolution of the flow similar to what would have been obtained for single phase cases with increasing Rayleigh number (Hay and Papalexandris, 2019; Kerr, 1996). Indeed, the convection, the heat transported throughout the domain (global Nusselt number), the turbulence intensity and the thermal mixing are all enhanced. At $Ja = 0$ (and other very small values), the trends are unusual and even contradictory: the convection decreases while the global heat transfer is improved and the thermal mixing is reinforced while turbulence is reduced. These effects may be explained by the meaning behind a null Jakob number. Indeed, when Jakob is zero, bubbles are able to exchange energy with the surrounding liquid but are never allowed to grow/shrink. The usual links between temperature and speed are thus broken by this purely theoretical condition.

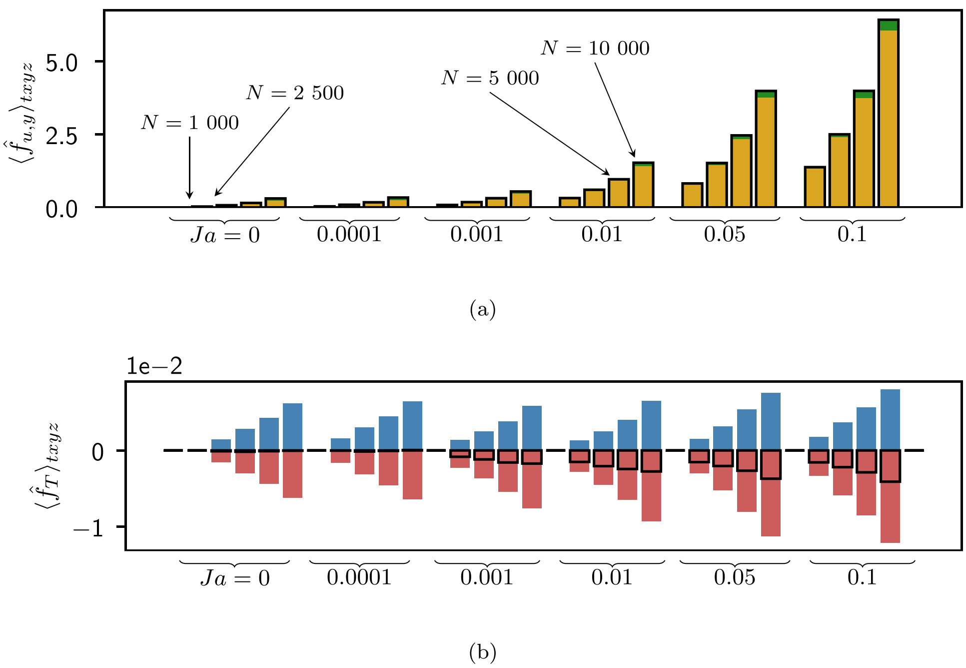

Fig. 22. Time and volume-averaged non-dimensional (a) momentum, $\hat{f}_{u,y}$ and (b) thermal, $\hat{f}_T$ effects for Jakob number ranging from 0 to 0.1 and containing 1000, 2500, 5000 or 10 000 bubbles (▭). The fields are filtered according to either the vertical direction of the surrounding liquid: rising (▬)/sinking (▬) or the surrounding liquid temperature : hot (▬)/cold (▬).

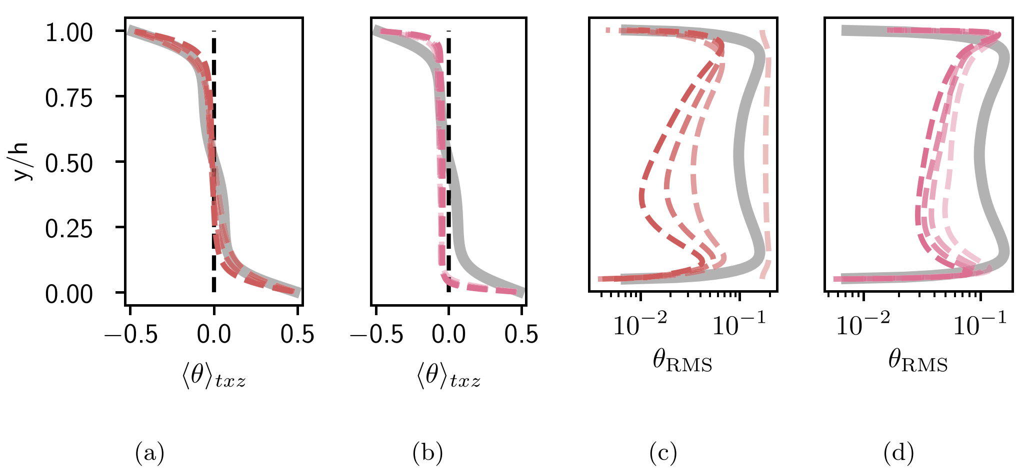

Fig. 23. Plots of the time and area-averaged normalized temperature, $\langle \theta \rangle_{txz}$ for (a) $Ja = 0$ and (b) $Ja = 0.1$ as well as of the RMS temperature for (c) $Ja = 0$ and (d) $Ja = 0.1$. Values for 1000, 2500, 5000 and 10 000 bubbles are displayed from lightest to darkest shades. The single phase case (▬) and the saturation temperature value, T_{sat} (▬ ▬ ▬) are added for comparison.

6. Steering Jakob's number

Until this section, cases have been defined by altering the latent heat to obtain the desired Jakob number. This method allows to keep the same temperature difference and height of the domain in order to obtain results that may be easily comparable. However, in reality, the latent heat is a characteristic of the fluid. A more physical way of defining cases (but less numerically practical) would therefore be to set the reference temperature, Rayleigh and Jakob numbers and to deduce the temperature difference and height that must be applied accordingly.

In order to assess how these method compare against one another, we take the previously detailed case characterized by a Jakob number of zero and 10 000 bubbles as a reference. The latter is summarized in the 1st line of Table 3. Even though this case is particular as it is always characterized by an infinite latent heat, it will allow a better/easier comparison as bubbles size is not able to change. We then define a new height and temperature difference combo which allows to obtain the same Rayleigh number. From there, three cases are defined, which all have the new height and temperature difference. The first one keeps both the same amount of bubbles and their initial radius. The second and third ones aim at preserving the same void fraction by adapting the initial radius and number of bubbles respectively. These new cases are detailed in Table 3.

Fig. 25 displays the various components constituting the time and volume averaged Nusselt number for the simulations understudy. Since the Rayleigh number is the same for all simulations, the diffusive term remains unchanged for all cases. Case 1, due to its decrease of the void fraction presents a lower value of the global Nusselt number. It also shows an slight enhancement of the convection term. Case 2 contains 10 000 bubbles which are bigger than in other cases, allowing

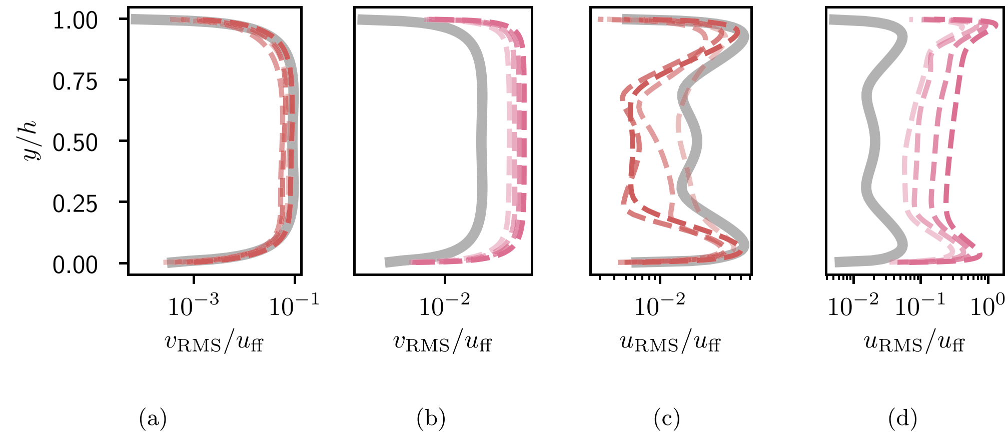

Fig. 24. Plots of the RMS non-dimensional vertical velocity for (a) $Ja = 0$ and (b) $Ja = 0.1$ as well as of the RMS non-dimensional horizontal velocity for (c) $Ja = 0$ and (d) $Ja = 0.1$. Values for 1000, 2500, 5000 and 10 000 bubbles are displayed from lightest to darkest shades. The single phase case ( ) is added for comparison.

Table 3
Cases description, all with $Ra = 2.12 \times 10^5$ and Jakob number $Ja = 0$: height of the domain h, temperature difference ΔT, latent heat h_{lv}, volume of the domain V_{tot}, number of bubbles N_b, initial radius size r_0, volume occupied by the bubbles V_b and void fraction V_b/V_{tot}.

	h	ΔT	h_{lv}	V_{tot}	N_b	r_0	V_b	V_b/V_{tot}
Ref. Case	$1.79e^{-2}$	0.25	∞	$1.43e^{-6}$	10 000	$12.5e^{-6}$	$8.18e^{-11}$	$5.72e^{-5}$
Case 1	$2.78e^{-2}$	$6.68e^{-2}$	∞	$5.36e^{-6}$	10 000	$12.5e^{-6}$	$8.18e^{-11}$	$1.53e^{-5}$
Case 2	$2.78e^{-2}$	$6.68e^{-2}$	∞	$5.36e^{-6}$	10 000	$19.4e^{-6}$	$3.07e^{-10}$	$5.72e^{-5}$
Case 3	$2.78e^{-2}$	$6.68e^{-2}$	∞	$5.36e^{-6}$	37 485	$12.5e^{-6}$	$3.07e^{-10}$	$5.72e^{-5}$

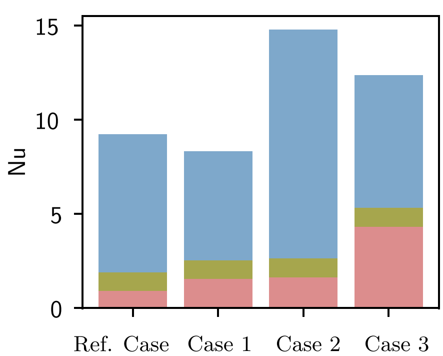

Fig. 25. Nusselt number for the simulations described in Table 3. Convection ( ), diffusion ( ) and bubble-related ( ) components of the volume-averaged Nusselt number.

to preserve the reference void fraction. As the bubbles are bigger, the bubble-related term is strongly enhanced while the convection one shows a slight increase. Lastly, case 3 contains 37 485 bubbles at the same reference initial radius. As compared to Case 1, the bubble related term is slightly enhanced while the convection one shows a significant growth.

These simulations have highlighted that the void fraction plays an important role but is not a sufficient parameter on its own. In fact, Fig. 25 shows that the Nusselt number is increased mainly through the convective term when bubbles are added, and through the bubble-related term when bubbles are larger. However, an infinite number of combinations of these two parameters can lead to the same void fraction as in the reference case. One of them may or may not lead to the same results as the reference case. One should also note that cases with a non-zero value of the Jakob number would be even more complex as the void fraction would not equal to the initial one and bubbles would not have the same size as they could grow and shrink.

7. Conclusion

In this paper, we presented simulations of Rayleigh–Bénard convection in the presence of growing/shrinking vapor bubbles in a cube. For this purpose, an Eulerian-Lagrangian model was used to track the bubble position, velocity and size, along with a two-way coupling methodology to account for the effect of bubbles on the fluid. The objective of this work was to study the convective structures of the flow of interest as well as the heat fluxes passing through the domain for different bubble parameters. Our simulations confirmed that the Jakob number, the amount of bubbles and their initial size have a strong impact on the flow.

First of all, when adding various amount of bubbles at different Jakob numbers, we observe two different flow structures. At low volume fractions, we find a “single diagonally oriented roll” (typical of classical RBC) and, at high volume fractions, an “almost toroïdal roll”. In the latter, the fluid rises along the four corners of the geometry and sinks in the middle. The transition from one structure to the other, although strongly dependent on the volume fraction, depends in a more subtle way on the manner the latter is imposed. Indeed, many small bubbles or few large bubbles impact the structure differently and can therefore influence towards one structure or the other.

At $Ja = 0$, bubbles are uniformly present in the flow, interacting with both superheated and sub-cooled fluid as well as ascending and descending fluid. Bubbles are not able to change size due to the infinite latent heat but exchange energy with the surrounding fluid, through an energy additional term f_T. These exchanges tend to make the surrounding liquid temperature converge towards the saturation temperature therefore lessening the temperature gradients, ergo convection inside the fluid phase. Bubbles also impact the flow through an additional momentum term, $\boldsymbol{f}_U$, which can be interpreted as a forced convection term driven by the upward movement of the bubbles, which promotes convection. At $Ja = 0$, the resultant of these two effects tends to reduce convection within the liquid. The overall Nusselt number, which may be decomposed into 3 terms: a convective term and a diffuse term as in classical Rayleigh–Bénard convection, plus a final term which accounts for the energy that the bubbles transport across the domain as they rise, is however increased. The diffusive component is unchanged as compared to single phase while the additional term coming from the bubbles counter-balances the decrease of convection. The cases therefore lead to a reduction in turbulent intensity and an improvement in thermal mixing, all the more important as the amount of bubbles is increased. One should also note that imposing $Ja = 0$ is a theoretical condition that isolates the mechanical and thermal impact of bubbles on the flow from radius variation effects. While this breaks the usual coupling between mass and energy transfer, it remains a useful reference case, helping to isolate the effects of buoyancy-driven motion from those induced by bubble growth or collapse.

As the Jakob number increases, bubbles grow and shrink more easily, allowing the vapor phase to concentrate in strategic locations, namely the four ascending plumes, which enables them to accelerate their ascent. Bubbles are therefore seen to grow with the Jakob number. The momentum effect is widely increased while the thermal effect is limited by the temperature spectrum. Both effects lead to an increase of convection as compared to cases at $Ja = 0$. The Nusselt number thus shows large increases coming from both the convective term and the term directly linked to the bubbles. Furthermore, turbulence statistics have shown an increase of the turbulence intensity and a better thermal mixing with increasing Jakob number and amount of bubbles. These effects are similar to those that would be obtained in the single-phase configuration when increasing the Rayleigh number.

The results obtained here illustrate the complexity of the flow studied. The flow appears to be characterized by the usual parameters of Rayleigh–Bénard convection, as well as the Jakob number, the degree of superheat (whose influence has not been studied here), the number of bubbles and their size. The large number of degrees of freedom to characterize the problem, combined with the coupling of the two phases, are at the root of this complexity. Added to this is the fact that the parameterization, found and used here, depends on case-specific parameters and is therefore not globally generalizable. A key point for further research into this type of flow would be to develop a parameterization of the problem that takes account of the size and number of bubbles, while remaining general.

In addition, this study shows us that there are a number of challenges to be overcome if we wish to push certain values further, such as the number of bubbles and the Jakob number. Indeed, the clustering of bubbles in the corners of the geometry increases the local values of the volume fractions, calling into question the assumption of neglecting bubble-bubble interactions or even of using an Eulerian-Lagrangian model. Furthermore, the model could be extended to take volumetric coupling into account, enabling better consideration of coupling effects between bubbles and liquid. Lastly, some studies have highlighted the fact that bubbles do not nucleate uniformly across the domain and the need to investigate the effects of preferential nucleation on flow (Schmidt et al., 2011; Guzman et al., 2016).

CRediT authorship contribution statement

Joauma Marichal: Writing – review & editing, Writing – original draft, Conceptualization. **Yann Bartosiewicz:** Writing – review & editing, Supervision. **Pierre Ruyer:** Writing – review & editing, Supervision.

Declaration of competing interest

The authors declare the following financial interests/personal relationships which may be considered as potential competing interests: Joauma Marichal reports equipment, drugs, or supplies was provided by Consortium des Equipements de Calcul Intensif en Fédération Wallonie Bruxelles (CECI). If there are other authors, they declare that they have no known competing financial interests or personal relationships that could have appeared to influence the work reported in this paper.

Acknowledgments

Computational resources have been provided by the supercomputing facilities of the Université catholique de Louvain (CISM/UCL) and the Consortium des Équipements de Calcul Intensif en Fédération Wallonie Bruxelles (CÉCI) funded by the Fond de la Recherche Scientifique de Belgique (F.R.S.-FNRS) under convention 2.5020.11 and by the Walloon Region.

The present research benefited from computational resources made available on Lucia, the Tier-1 supercomputer of the Walloon Region, infrastructure funded by the Walloon Region under the grant agreement n°1910247.

Table A.4
Additional cases at $Ja = 0$: bubble void fraction, ϕ_b, number of bubbles N_b, bubble radii $r_{b,0}$ and grid resolution $N_x \times N_y \times N_z$.

ϕ_b	N_b	$r_{b,0}$ [μm]	$N_x \times N_y \times N_z$
$5.71e^{-6}$	2500	9.21	$50 \times 70 \times 50$
$5.71e^{-6}$	5000	7.31	$50 \times 70 \times 50$
$5.71e^{-6}$	10 000	5.80	$50 \times 70 \times 50$
$1.43e^{-5}$	1000	16.97	$50 \times 70 \times 50$
$1.43e^{-5}$	5000	9.92	$50 \times 70 \times 50$
$1.43e^{-5}$	10 000	7.87	$50 \times 70 \times 50$
$5.71e^{-5}$	1000	26.93	$50 \times 70 \times 50$
$5.71e^{-5}$	2500	19.84	$50 \times 70 \times 50$
$5.71e^{-5}$	5000	15.75	$50 \times 70 \times 50$

Appendix A. Additional cases at $Ja = 0$

See Table A.4.

Appendix B. Nusselt number

The Nusselt number, i.e. the average vertical heat flux through the domain, can be obtained by integrating the energy equation under certain conditions: no-slip and adiabatic boundaries on the sides, a no-slip bottom boundary and a statistically steady state. As seen previously, the energy equation (Eq. (3)) is given by,

$$\frac{\partial(\rho c_p T)}{\partial t} + \nabla\cdot\left(\rho c_p \boldsymbol{u} T\right) = \frac{\partial p_0(t)}{\partial t} + \nabla\cdot(\kappa\nabla T) + f_T\,.$$

In order to derive an expression for the Nusselt number, we integrate over the horizontal directions $(x,\, z)$ and the time (t):

$$\begin{aligned}\int_x\int_z\int_t\Big(\frac{\partial(\rho c_p T)}{\partial t} + \nabla\cdot\left(\rho c_p \boldsymbol{u} T\right)\Big)dx\,dz\,dt \\ = \int_x\int_z\int_t\Big(\frac{\partial p_0(t)}{\partial t} + \nabla\cdot(\kappa\nabla T) + f_T\Big)dx\,dz\,dt + C\,.\end{aligned} \tag{B.1}$$

As we consider a statistically steady state (i.e. $\langle\frac{\partial a}{\partial t}\rangle_t = 0$), we obtain,

$$\int_x\int_z\int_t \nabla\cdot\left(\rho c_p \boldsymbol{u} T\right)dx\,dz\,dt = \int_x\int_z\int_t\Big(\nabla\cdot(\kappa\nabla T) + f_T\Big)dx\,dz\,dt + C\,.$$

Furthermore, the convective term, can be reexpressed as,

$$\begin{aligned}&\int_x\int_z\int_t \nabla\cdot\left(\rho c_p \boldsymbol{u} T\right)dx\,dz\,dt \\ &= \int_x\int_z\int_t\left(\frac{d}{dx}(\rho c_p u_x T) + \frac{d}{dy}(\rho c_p u_y T) + \frac{d}{dz}(\rho c_p u_z T)\right)dx\,dz\,dt\,,\end{aligned}$$

where the horizontal derivatives are equal to zero due to the adiabatic side walls ($\boldsymbol{u} = 0$):

- $\int_x\int_z\int_t \frac{d}{dx}(\rho c_p u_x T)dx\,dz\,dt = \int_z\int_t[(\rho c_p u_x T)]_{x=0}^{x=h}dz\,dt = 0,$
- $\int_x\int_z\int_t \frac{d}{dz}(\rho c_p u_z T)dx\,dz\,dt = \int_x\int_t[(\rho c_p u_z T)]_{z=0}^{z=h}dx\,dt = 0.$

Following a similar approach for the diffusive term, we obtain,

$$\begin{aligned}&\int_x\int_z\int_t \nabla\cdot(\kappa\nabla T)\,dx\,dz\,dt \\ &= \int_x\int_z\int_t\left(\frac{d}{dx}\left(\kappa\frac{dT}{dx}\right) + \frac{d}{dy}\left(\kappa\frac{dT}{dy}\right) + \frac{d}{dz}\left(\kappa\frac{dT}{dz}\right)\right)dx\,dz\,dt\,,\end{aligned}$$

where the horizontal derivatives are equal to zero due to the adiabatic side walls ($\frac{dT}{dx} = \frac{dT}{dz} = 0$):

- $\int_x\int_z\int_t \frac{d}{dx}(\kappa\frac{dT}{dx})dx\,dz\,dt = \int_z\int_t[\kappa\frac{dT}{dx}]_{x=0}^{x=h}dz\,dt = 0,$
- $\int_x\int_z\int_t \frac{d}{dz}(\kappa\frac{dT}{dz})dx\,dz\,dt = \int_x\int_t[\kappa\frac{dT}{dz}]_{z=0}^{z=h}dx\,dt = 0.$

Eq. (B.1) is therefore equivalent to,

$$\int_x\int_z\int_t \frac{d}{dy}(\rho c_p u_y T)dx\,dz\,dt = \int_x\int_z\int_t\left(\frac{d}{dy}\left(\kappa\frac{dT}{dy}\right) + f_T\right)dx\,dz\,dt + C\,.$$

As we are working on a discrete grid, we get,

$$\left\langle \frac{d}{dy}(\rho c_p u_y T) \right\rangle_{xzt} = \left\langle \frac{d}{dy}\left(\kappa \frac{dT}{dy}\right) \right\rangle_{xzt} + \left\langle f_T \right\rangle_{xzt} + C . \tag{B.2}$$

To derive an expression for the Nusselt number, Eq. (B.2) must still be integrated in the vertical direction:

$$\int_0^y \left\langle \frac{d}{dy}(\rho c_p u_y T) \right\rangle_{xzt} dy = \int_0^y \left\langle \frac{d}{dy}\left(\kappa \frac{dT}{dy}\right) \right\rangle_{xzt} dy + \int_0^y \left\langle f_T \right\rangle_{xzt} dy + C' .$$

Since the bottom boundary has a no-slip condition, the equation gives, in discrete form,

$$\langle \rho c_p u_y T \rangle_{xzt}|_y = \left\langle \kappa \frac{dT}{dy} \right\rangle_{xzt}\Big|_y - \left\langle \kappa \frac{dT}{dy} \right\rangle_{xzt}\Big|_0 + \int_0^y \langle f_T \rangle_{xzt} dy + C' . \tag{B.3}$$

Finally, the equation is divided by $\frac{\kappa_{\text{ref}} \Delta T}{l_{\text{ref}}}$ (for non-dimensionalization purposes) and the constant terms "identified" as the **area-averaged Nusselt number**,

$$Nu_{\text{area}} = \frac{l_{\text{ref}}}{\kappa_{\text{ref}} \Delta T} \langle \rho c_p u_y T \rangle_{xzt}|_y - \frac{l_{\text{ref}}}{\kappa_{\text{ref}} \Delta T} \left\langle \kappa \frac{dT}{dy} \right\rangle_{xzt}\Big|_y - \frac{l_{\text{ref}}}{\kappa_{\text{ref}} \Delta T} \int_0^y \langle f_T \rangle_{xzt} dy . \tag{B.4}$$

To obtain the volume averaged Nusselt number, one must integrate one more time in the vertical direction (from 0 to l_{ref}), starting from Eq. (B.3):

$$\int_0^{l_{\text{ref}}} \langle \rho c_p u_y T \rangle_{xzt}|_y dy = \int_0^{l_{\text{ref}}} \left\langle \kappa \frac{dT}{dy} \right\rangle_{xzt}\Big|_y dy - \int_0^{l_{\text{ref}}} \left\langle \kappa \frac{dT}{dy} \right\rangle_{xzt}\Big|_0 dy + \int_0^{l_{\text{ref}}} \int_0^y \langle f_T \rangle_{xzt} dy' \, dy + C" .$$

Considering that κ is constant and equal to κ_{ref} (otherwise we should call on an integration function), we obtain,

$$l_{\text{ref}} \langle \rho c_p u_y T \rangle_{xyzt} = -\kappa_{\text{ref}} \Delta T - l_{\text{ref}} \left\langle \kappa \frac{dT}{dy} \right\rangle_{xzt}\Big|_0 - \int_0^{l_{\text{ref}}} \int_0^y \langle f_T \rangle_{xzt} dy' \, dy , \tag{B.5}$$

the equation is divided by $\kappa_{\text{ref}} \Delta T$ (again for non-dimensionalization purposes) and the constant terms "identified" as the **volume-averaged Nusselt number**,

$$Nu_{\text{vol}} = \frac{l_{\text{ref}}}{\kappa_{\text{ref}} \Delta T} \langle \rho c_p u_y T \rangle_{xyzt} + 1 - \int_0^{l_{\text{ref}}} \int_0^y \langle f_T \rangle_{xzt} dy' \, dy . \tag{B.6}$$

Non-dimensionalizing the fields allows to obtain Eq. (23).

Data availability

Data will be made available on request.

References

Auton, T.R., Hunt, J.C.R., Prud'Homme, M., 1988. The force exerted on a body in inviscid unsteady non-uniform rotational flow. J. Fluid Mech. 197, 241–257.

Bonnefis, P., Fabre, D., Magnaudet, J., 2023. When, how, and why the path of an air bubble rising in pure water becomes unstable. P. Natl. A. Sci. 120 (11), e2300897120.

Cioni, S., Ciliberto, S., Sommeria, J., 1996. Experimental study of high-Rayleigh-number convection in mercury and water. Dynam. Atmos. Ocean. 24 (1), 117–127.

Cioni, S., Ciliberto, S., Sommeria, J., 1997. Strongly turbulent Rayleigh–Bénard convection in mercury: comparison with results at moderate Prandtl number. J. Fluid Mech. 335, 111–140.

Darmana, D., Deen, N.G., Kuipers, J.A.M., 2006. Parallelization of an Euler–Lagrange model using mixed domain decomposition and a mirror domain technique: Application to dispersed gas–liquid two-phase flow. J. Comput. Phys. 220 (1), 216–248.

Deen, N.G., van Sint Annaland, M., Kuipers, J.A.M., 2004. Multi-scale modeling of dispersed gas–liquid two-phase flow. Chem. Eng. Sci. 59 (8), 1853–1861.

Dergarabedian, P., 1960. Observations on bubble growths in various superheated liquids. J. Fluid Mech. 9 (1), 39–48.

Elghobashi, S., 1994. On predicting particle-laden turbulent flows. Appl. Sci. Res. 52, 309–329.

Favre, L., 2023. Modélisation et Simulation de la Crise d'Ébullition dans les REP à l'Échelle CFD (Ph.D. thesis). Institut National Polytechnique de Toulouse.

Ferrante, A., Elghobashi, S.E., 2007. On the effects of microbubbles on Taylor–Green vortex flow. J. Fluid Mech. 572, 145–177.

Foroozani, N., Niemela, J., Armenio, V., Sreenivasan, K., 2017. Reorientations of the large-scale flow in turbulent convection in a cube. Phys. Rev. E 95, 033107.

Ganguli, A.A., Kenig, E.Y., 2011. A CFD-based approach to the interfacial mass transfer at free gas–liquid interfaces. Chem. Eng. Sci. 66 (14), 3301–3308.

Gennari, G., Smith, E., Pringle, G., Magnini, M., 2024. A hybrid atomistic-continuum framework for multiscale simulations of boiling. J. Phys. Conf. Ser. 2766, 012151.

Grötzbach, G., 1983. Spatial resolution requirements for direct numerical simulation of the Rayleigh–Bénard convection. J. Comput. Phys. 49 (2), 241–264.

Guzman, D.N., Xie, Y., Chen, S., Rivas, D.F., Sun, C., Lohse, D., Ahlers, G., 2016. Heat-flux enhancement by vapour-bubble nucleation in Rayleigh–Bénard turbulence. J. Fluid Mech. 787, 331–366.

Hamtiaux, V., 2024. Numerical Simulation of Natural Convection in Mixed Porous/Pure-Fluid Domains (Ph.D. thesis). UCL - Université Catholique de Louvain.

Hay, W.H., Martin, J., Migot, B., Papalexandris, M.V., 2021. Turbulent thermal convection driven by free-surface evaporation in cuboidal domains of different aspect ratios. Phys. Fluids 33, 015104.

Hay, W.A., Papalexandris, M.V., 2019. Numerical simulations of turbulent thermal convection with a free-slip upper boundary. Proc. R. Soc. A 475, 20190601.

Juric, D., Tryggvason, G., 1998. Computations of boiling flows. Int. J. Multiphas. Flow 24 (3), 387–410.

Kerr, R.M., 1996. Rayleigh number scaling in numerical convection. J. Fluid Mech. 310, 139–179.

Krishnamurti, R., Howard, L.N., 1981. Large-scale flow generation in turbulent convection. Proc. Natl. Acad. Sci. USA 78 (4), 1981—1985.

Lakkaraju, R., Boiling Turbulent Rayleigh–Bénard Convection (Ph.D. thesis). University of Twente, Enschede, The Netherlands.

Legendre, D., Borée, J., Magnaudet, J., 1998. Thermal and dynamic evolution of a spherical bubble moving steadily in a superheated liquid. Phys. Fluids 10, 1256–1272.

Lemmon, E.W., Huber, M.L., McLinden, M.O., 2010. NIST Standard Reference Database 23: Reference Fluid Thermodynamic and Transport Properties - REFPROP, ninth ed..

Lessani, B., Nakhaei, M.H., 2013. Large-eddy simulation of particle-laden turbulent flow with heat transfer. Int. J. Heat Mass Transfer 67, 974–983.

Magnaudet, J., 1997. The forces acting on bubbles and rigid particles.

Magnaudet, J., Rivero, M., Fabre, J., 1995. Accelerated flows past a rigid sphere or a spherical bubble. Part 1. Steady straining flow. J. Fluid Mech. 284, 97–135.

Martin, J., Ruyer, P., Duponcheel, M., Bartosiewicz, Y., 2023. A novel experimental observation of the gravity-driven flashing of metastable water in a heated pool. Nucl. Eng. Des. 410, 112371.

Maxey, M.R., Riley, J.J., 1983. Equation of motion for a small rigid sphere in a nonuniform flow. Phys. Fluids 26 (4), 883–889.

Mazzitelli, I.M., Lohse, D., Toschi, F., 2003. On the relevance of the lift force in bubbly turbulence. J. Fluid Mech. 488, 283–313.

Mei, R., Klausner, J., 1992. Unsteady force on a spherical bubble at finite Reynolds number with small fluctuations in the free-stream velocity. Phys. Fluids 4, 63–70.

Mei, R., Klausner, J.F., Lawrence, C.J., 1994. A note on the history force on a spherical bubble at finite Reynolds number. Phys. Fluids 6 (1), 418–420.

Niemela, J., Skrbek, L., Sreenivasan, K., Donnelly, R., 2000. Turbulent convection at very high Rayleigh numbers. Nature 404, 837–840.

Oresta, P., Lohse, D., Prosperetti, A., 2009. Heat transfer mechanisms in bubbly Rayleigh–Benard convection. Phys. Rev. E 80, 026304.

Paillere, H., Viozat, C., Kumbaro, A., Toumi, I., 2000. Comparison of low Mach number models for natural convection problems. Heat Mass Transf. 36 (6), 567–573.

Pallarès, J., Arroyo, M., Grau, F.X., Giralt, F., 2001. Experimental laminar Rayleigh–Bénard convection in a cubical cavity at moderate Rayleigh and Prandtl numbers. Exp. Fluids 31, 208–218.

Pallares, J., Cuesta, I., Arroyo, M., Grau, F.X., Giralt, F., 1996. Natural convection in a cubical cavity heated from below at low Rayleigh numbers. Int. J. Heat Mass Transfer 39, 3233–3247.

Plesset, M.S., Zwick, S.A., 1954. The growth of vapor bubbles in superheated liquids. J. Appl. Phys. 25 (493), 493–500.

Pope, S.B., 2000. Turbulent Flows. Cambridge University Press, Cambridge.

Rhie, C.M., Chow, W.L., 1983. Numerical study of the turbulent flow past an airfoil with trailing edge separation. AIAA 21 (11), 1525–1532.

Schmidt, L.E., Oresta, P., Toschi, F., Verzicco, R., Lohse, D., Prosperetti, A., 2011. Modification of turbulence in Rayleigh–Bénard convection by phase change. New J. Phys. 13 (2), 025002.

Shams, E., 2009. Numerical Simulation of Cavitating Bubble-Laden Turbulent Flows (Ph.D. thesis). University of Twente.

Shams, E., Finn, J., Apte, S.V., 2011. A numerical scheme for Euler–Lagrange simulation of bubbly flows in complex systems. Int. J. Numer. Methods Flow 67 (12), 1865–1898.

Shishkina, O., Stevens, R.J.A.M., Grossmann, S., Lohse, D., 2010. Boundary layer structure in turbulent thermal convection and its consequences for the required numerical resolution. New J. Phys. 12 (7), 075022.

Taylor, G.I., Green, A.E., 1937. Mechanism of the production of small eddies from large ones. Proc. R. Soc. Lond. A Mat. 158 (895), 499–521.

Tomiyama, A., Žun, I., Higaki, H., Makino, Y., Sakaguchi, T., 1997. A three-dimensional particle tracking method for bubbly flow simulation. Nucl. Eng. Des. 175 (1), 77–86.

Vishnu, V.T., De, A.K., Mishra, P.K., 2020. Dynamics of large-scale circulation and energy transfer mechanism in turbulent Rayleigh–Bénard convection in a cubic cell. Phys. Fluids 32 (9), 095115.

Zhou, Q., Xia, K.-Q., 2013. Thermal boundary layer structure in turbulent Rayleigh–Bénard convection in a rectangular cell. J. Fluid Mech. 721, 199–224.